Micro–X-ray fluorescence (μXRF) analysis of proximal impactites: High-resolution element mapping, digital image analysis, and quantifications

Kaskes, Pim; Déhais, Thomas; de Graaff, Sietze J.; Goderis, Steven; Claeys, Philippe

Published in:
Geological Society Special Publications

DOI:
10.1130/2021.2550(07)

Publication date:
2021

The Geological Society of America
Special Paper 550

Micro–X-ray fluorescence (μXRF) analysis of proximal impactites: High-resolution element mapping, digital image analysis, and quantifications

Pim Kaskes*
Thomas Déhais*
Sietze J. de Graaff
Analytical, Environmental & Geo-Chemistry Research Unit, Department of Chemistry, Vrije Universiteit Brussel (AMGC-WE-VUB), Pleinlaan 2, 1050 Brussels, Belgium, and
Laboratoire G-Time, Université Libre de Bruxelles, Avenue F.D. Roosevelt 50, 1050 Brussels, Belgium

Steven Goderis
Philippe Claeys
Analytical, Environmental & Geo-Chemistry Research Unit, Department of Chemistry, Vrije Universiteit Brussel (AMGC-WE-VUB), Pleinlaan 2, 1050 Brussels, Belgium

ABSTRACT

Quantitative insights into the geochemistry and petrology of proximal impactites are fundamental to understand the complex processes that affected target lithologies during and after hypervelocity impact events. Traditional analytical techniques used to obtain major- and trace-element data sets focus predominantly on either destructive whole-rock analysis or laboratory-intensive phase-specific micro-analysis. Here, we present micro–X-ray fluorescence (μXRF) as a state-of-the-art, time-efficient, and nondestructive alternative for major- and trace-element analysis for both small and large samples (up to 20 cm wide) of proximal impactites. We applied μXRF element mapping on 44 samples from the Chicxulub, Popigai, and Ries impact structures, including impact breccias, impact melt rocks, and shocked target lithologies. The μXRF mapping required limited to no sample preparation and rapidly generated high-resolution major- and trace-element maps (~1 h for 8 cm², with a spatial resolution of 25 μm). These chemical distribution maps can be used as qualitative multi-element maps, as semiquantitative single-element heat maps, and as a basis for a novel image analysis workflow quantifying the modal abundance, size, shape, and degree of sorting of segmented components. The standardless fundamental parameters method was used to quantify the μXRF maps, and the results were compared

*Kaskes and Déhais contributed equally to this study. Corresponding author e-mail addresses: pim.kaskes@vub.be (Kaskes), thomas.dehais@vub.be (Déhais).

Kaskes, P., Déhais, T., de Graaff, S.J., Goderis, S., and Claeys, P., 2021, Micro–X-ray fluorescence (μXRF) analysis of proximal impactites: High-resolution element mapping, digital image analysis, and quantifications, *in* Reimold, W.U., and Koeberl, C., eds., Large Meteorite Impacts and Planetary Evolution VI: Geological Society of America Special Paper 550, p. 171–206, https://doi.org/10.1130/2021.2550(07).

with bulk powder techniques. Concentrations of most major elements (Na_2O–CaO) were found to be accurate within 10% for thick sections. Overall, we demonstrate that μXRF is more than only a screening tool for heterogeneous impactites, because it rapidly produces bulk and phase-specific geochemical data sets that are suitable for various applications within the earth sciences.

INTRODUCTION

Impactites represent unique lithologies formed as the result of hypervelocity impact events on terrestrial planetary bodies (Stöffler and Grieve, 2007). The nature and emplacement of impactites are unequivocally related to the shock dynamics (e.g., size of the impactor), type of environment (oceanic vs. continental), and the target stratigraphy, which can be homogeneous or heterogeneous (Osinski et al., 2008). Impactites are subdivided into distal (at >2.5 crater diameter distance) and proximal impactites (Glass and Simonson, 2012), where the latter are found both within the crater as part of the continuous ejecta blanket at a distance of less than 2.5 times the crater diameter (Stöffler and Grieve, 2007). Proximal impactites are further subdivided into shocked target rocks, impact melt rocks, and impact breccias (Stöffler and Grieve, 2007). Shocked target rocks are nonbrecciated, melt-free rocks displaying unequivocal effects of shock metamorphism. Studies of their petrography and geochemical composition provide important constraints on the degree of shock and deformation that occurred within the crater (Melosh, 1989; French, 1998; Riller et al., 2018).

Impact melt rocks result from impact melting (Dressler and Reimold, 2001) and represent the solidified state of molten target rocks (Stöffler and Grieve, 2007). They vary from clast-rich to clast-free and mostly occur within impact structures in the form of coherent impact melt sheets emplaced on the crater floor (Grieve and Therriault, 2012). The geochemical and isotopic signatures of impact melt rocks are unique to every impact crater, as they depend on the nature and contribution of distinct target lithologies and the impactor (French, 1998). Based on both geochemical (e.g., Floran et al., 1978; Jahn et al., 1978; von Engelhardt and Graup, 1984) and theoretical (e.g., Simonds and Kieffer, 1993) data, impact melt rocks are considered to be geochemically homogeneous. However, this homogeneity applies essentially to major-element compositions, as trace-element concentrations (Reimold et al., 1990) and isotope ratios (e.g., Marchand and Crocket, 1977; Kettrup et al., 2003) are known to display considerable variability within impact melt rocks. This variability relates to target heterogeneity and/or dissimilar contributions of distinct target rocks incorporated at the local scale after turbulent motion of the melt (Kettrup et al., 2003; Thompson and Spray, 2017).

Impact breccias are classified according to the contribution of a single target lithology or multiple target lithologies (monomict vs. polymict breccias) and the absence or presence of impact melt particles within the matrix, with classification as a lithic breccia or suevite, respectively. Suevite is a polymict impact melt–bearing breccia with a particulate matrix containing fragments of shocked and unshocked mineral and lithic clasts (Stöffler, 1977; Stöffler and Grieve, 2007). In the case of suevite, the depositional mechanisms remain relatively poorly understood, and formational scenarios range from ground-hugging density currents (Siegert et al., 2017) to fallback following the collapse of the ejecta plume (Wittmann et al., 2007), ocean resurge within the crater (Ormö et al., 2007; Gulick et al., 2019), and phreatomagmatic (molten fuel coolant) interaction (Grieve et al., 2010; Artemieva et al., 2013; Osinski et al., 2020).

Due to the target lithology heterogeneities and their chaotic formational processes, proximal impactites are complex rocks that appear to be bound to crater-specific conditions. Their petrological and geochemical characterization sheds light on those parts of the target stratigraphy that were brecciated, melted, or shock-vaporized as a result of the impact. This knowledge can be used to reconstruct the pressure and temperature conditions under which proximal impactites formed (Melosh, 1989; French, 1998).

While macroscopic and microscopic observations aid in identifying the different mineralogic components within these impactites, such petrographic techniques lack insights into specific chemical variations both at the bulk level and between clasts and/or groundmass. Several analytical techniques generate accurate and precise concentrations of major and trace elements in geological samples. However, these are either destructive techniques based on solutions and powders (such as inductively coupled plasma–mass spectrometry [ICP-MS], inductively coupled plasma–optical emission spectrometry [ICP-OES], instrumental neutron activation analysis [INAA], and bulk glass bead X-ray fluorescence [XRF]) or semidestructive in situ techniques based on thin and/or thick sections (such as electron microprobe analysis [EMPA], laser ablation–inductively coupled plasma–mass spectrometry [LA-ICP-MS], and synchrotron-based XRF). All these techniques require time-consuming and/or laborious sample preparation, especially in the case of the in situ techniques. Micro–X-ray fluorescence (hereafter μXRF) is a powerful tool to overcome these problems because this technique causes very limited to no damage to a sample, and it can rapidly produce bulk elemental data sets. In addition, μXRF makes it possible to visualize and quantify chemical heterogeneity at a high spatial resolution (down to 20 μm) within a sample (de Winter and Claeys, 2017; Flude et al., 2017).

The usefulness of μXRF methodologies in the context of distal impactites has already been demonstrated, both in the case of Archean spherule layers (e.g., Goderis et al., 2013a; Hoehnel

et al., 2018; Huber et al., 2019) and Cenozoic ejecta materials, including Australasian tektites (e.g., Goderis et al., 2017). In this study, we explored the potential of μXRF as a fast, inexpensive, and nondestructive technique particularly suitable to the study of proximal impactites. Additionally, μXRF constitutes an ideal approach to select optimal sample locations and prepare these phases for more detailed analysis such as LA-ICP-MS, especially in the case of rare, important, or highly heterogeneous samples, as impactites often are (e.g., scarce drill core intervals, impactites with meteoritic contributions, or fragile impact glass with possible clay alteration). We demonstrate the potential of high-resolution, qualitative to semiquantitative element mapping followed by quantitative digital image analysis based on these μXRF maps. Furthermore, we quantified a range of different impactite lithologies and compared the measured compositions with those determined by bulk powder–based techniques on the same samples. The methodology and case studies presented here highlight the advantages of μXRF to rapidly and efficiently document the composition of heterogeneous and proximal products from impact structures.

MATERIALS AND METHODS

Sample Selection

In total, 44 samples from the Chicxulub, Ries, and Popigai impact structures were selected to illustrate the three main types of proximal impactites, i.e., shocked target rocks, impact melt rocks, and impact breccias. These impact structures range in diameter from ~24 km to ~180 km and represent structures formed on distinctly different geological settings, with varying complexities of target lithologies that range from magmatic to metamorphic and/or sedimentary in origin.

The Chicxulub impact structure (Yucatán, Mexico) is ~180 km in diameter (Hildebrand et al., 1991). It has been dated at 66.052 ± 0.008/0.043 Ma and coincides with the Cretaceous-Paleogene boundary mass extinction (Sprain et al., 2018). The Chicxulub crater is the result of the impact of a 10 ± 4 km diameter (Alvarez et al., 1980) carbonaceous chondrite (Goderis et al., 2013b) on a Mesozoic carbonate and evaporite platform, which rests on crystalline target rocks ranging from Neoproterozoic age (ca. 546 Ma; Keppie et al., 2011; Renne et al., 2013) to Carboniferous age (326 ± 5 Ma; Zhao et al., 2020). The 40 Chicxulub samples used in this study originated from the International Ocean Discovery Program–International Continental Drilling Project (IODP-ICDP) Expedition 364 drill core: 9 crystalline target rocks, 21 impact melt rocks, and 10 impact breccias (Fig. 1A). This core was drilled offshore on the Chicxulub peak ring at Site M0077 (global positioning system [GPS] coordinates: 21.45°N, 89.95°W in World Geodetic System 1984 [WGS84] reference coordinate system) in 2016 and reached a depth of 1334.7 m below seafloor (mbsf; Morgan et al., 2016). This drilling extracted a near-continuous sequence of proximal impactites consisting of ~104 m of suevite, ~26 m of impact melt rocks, and ~610 m of granitoid basement material intruded by pre-impact mafic dikes and suevite/impact melt rock (e.g., Morgan et al., 2017; Kring et al., 2017). In the Expedition 364 drill core, the peak-ring lithologies all display pervasive hydrothermal alteration (Kring et al., 2020; Simpson et al., 2020).

The Ries impact structure (Germany) is an ~24-km-diameter impact structure (Pohl et al., 1977) with an age of 14.808 ± 0.021 Ma determined by ^{40}Ar-^{39}Ar (Schmieder et al., 2018; Schmieder and Kring, 2020). The target at the Ries structure is composed of a Hercynian crystalline basement covered by Mesozoic sedimentary rocks (Schmidt-Kaler, 1978). The basement consists of gneisses, amphibolites, and ultrabasic rocks with granitic intrusions. The sedimentary sequence is constituted by sandstone, siltstone, marl, and limestone (Pohl et al., 1977). Two samples were selected from the Ries impact structure: impact melt rock sample Pols-01 and suevite sample Aum-01 (Fig. 1A). Pols-01 was sampled in 2008 at Polsingen (GPS coordinates [WGS84]: 48.92°N, 10.71°E), which is the location of one of the few outcrops in the Ries impact structure displaying isolated small (<100 m) lumps of coherent impact melt rock (Pohl et al., 1977; Graup, 1999). This represents one of the two main forms of impact-melted materials in the Ries crater; the other type constitutes impact melt particles within suevites (Osinski, 2003; Stöffler et al., 2013). Suevite sample Aum-01 was sampled in 2008 in the Aumühle quarry, near Oettingen (GPS coordinates [WGS84]: 48.97°N, 10.63°E), which yield several well-exposed suevite sections (Osinski et al., 2004). In the Ries impact structure, impact melt rock and suevite are characterized by the same stratigraphic position as they both overlie the sedimentary Bunte Breccia following a sharp contact (Hörz et al., 1983; Stöffler et al., 2013).

The Popigai impact structure (northern Siberia, Russia) is ~100 km in diameter (Masaitis, 1994) and has been dated to 36.63 ± 0.92 Ma using the ^{40}Ar-^{39}Ar step-heating technique (Schmieder and Kring, 2020). Popigai is part of a late Eocene cluster of impact structures, and it likely formed through the impact of a type L or H ordinary chondrite (Tagle and Claeys, 2005; Kyte et al., 2011) on the Archean Anabar Shield. The target at the Popigai impact crater site is composed of Archean to early Proterozoic crystalline rocks that are covered by sedimentary sequences (Masaitis, 1994). The latter include Proterozoic to Cambrian conglomerates, quartzites, dolomites, and limestones, Permian terrestrial sandstones and argillites, and discontinuous thin beds of Cretaceous sandstones (Vishnevsky and Montanari, 1999). Popigai has been determined to be the source crater of the late Eocene clinopyroxene microkrystite spherule layer (Liu et al., 2009). Within the crater, the shocked target rocks are covered by an ~2-km-thick impactite sequence composed of three main units that vary in thickness within the crater (Naumov, 2002; Masaitis et al., 2005). The lower unit includes polymict breccia constituted of fragments from the different target lithologies; the intermediate unit contains alternating impact melt rock (tagamite in the Russian literature) and suevite sheets; and the upper unit presents suevite lithology (Masaitis et al., 2005). The suevites from the intermediate and upper units mainly differ in

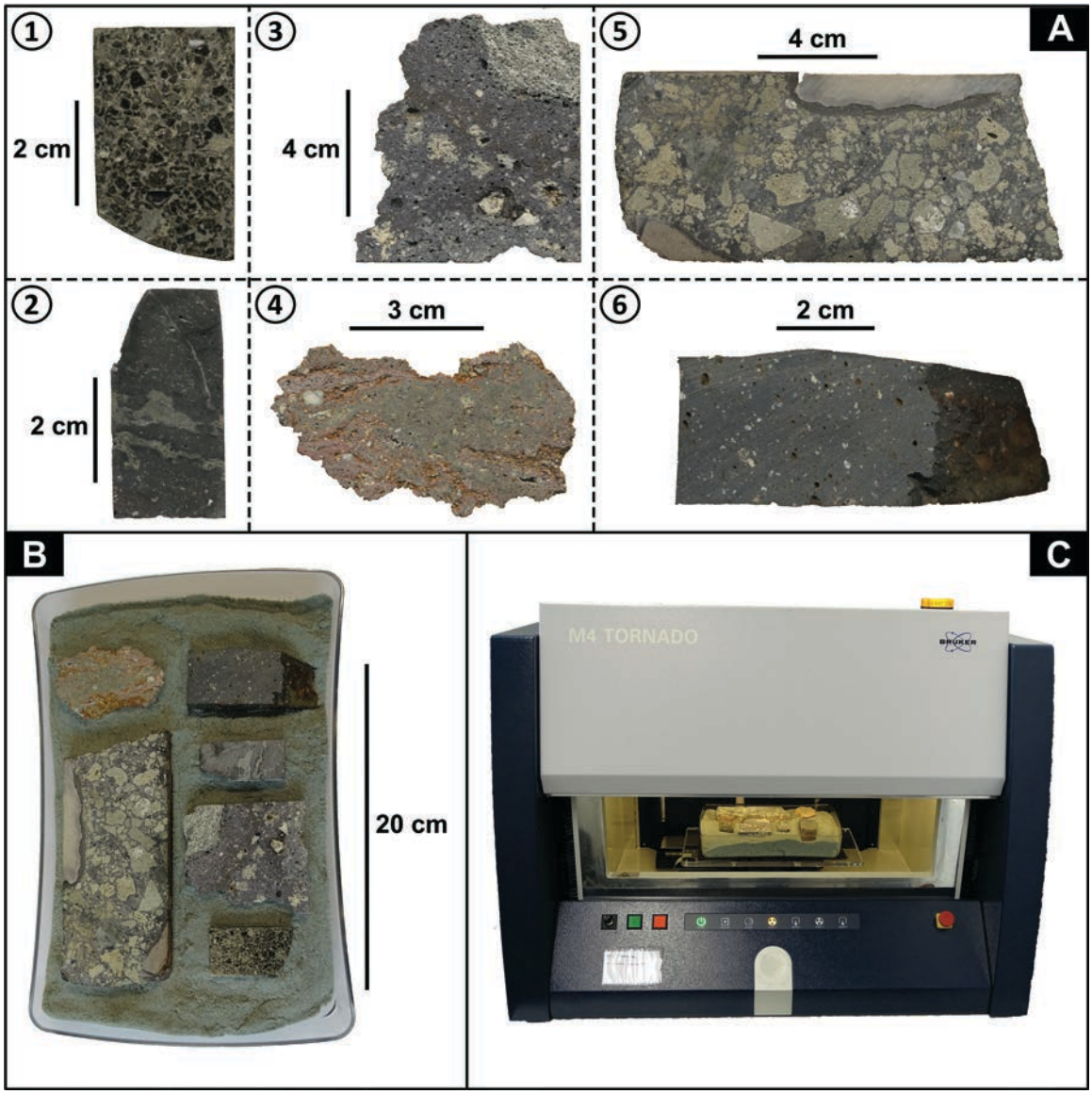

Figure 1. (A) Photographs of the samples: ① a suevite 54_1_64_66 and ② an impact melt rock 90_1_85_87 from the Chicxulub International Ocean Discovery Program–International Continental Drilling Project (IODP-ICDP) Expedition 364 drill core, Yucatán, Mexico; ③ a suevite Aum-01 and ④ an impact melt rock Pols-01 from Ries crater, Germany; ⑤ an impact breccia Pop C6 and ⑥ an impact melt rock Pop 10 from Popigai, northern Siberia, Russia. (B) Photograph of the samples loaded into the plastic holder filled with kinetic sand. The corresponding micro–X-ray fluorescence (μXRF) map is shown in Figure 4. (C) Photograph of the Bruker M4 Tornado μXRF instrument installed at the Analytical, Environmental & Geo-Chemistry Research Unit, Vrije Universiteit Brussel (AMGC-VUB), with samples loaded in the vacuum chamber.

the contained impact melt clasts (vitroclasts), which are black and greenish-gray, respectively (Naumov, 2002). Two samples were selected from the Popigai impact structure: an impact melt rock Pop 10 (from Tagle and Claeys, 2005) and an impact breccia Pop C6 (Fig. 1A). Both samples were collected during the International Expedition in 1997. Pop 10 was sampled from a large outcrop of impactites along the Rossokhe River, west of the crater (GPS coordinates [WGS84]: 71.76°N, 110.25°E; Tagle and Claeys, 2005). Pop C6 was collected northwest of the crater along the Rossokhe River and was sampled from a pile of scattered and abandoned old cores that were drilled in Popigai during the intense exploration programs by the Union of Soviet Socialist Republics (USSR) in the 1970s and 1980s (Masaitis et al., 2005).

Sample Preparation

Because the μXRF measurements are performed on a horizontal plane, the measured surface needs to be as flat as possible.

Naturally formed near-flat surfaces can directly be analyzed in the case of precious samples. However, preferably, rock samples are cut using a diamond board table saw and slightly polished to remove traces of contamination from the sawing blade (e.g., W, Co, Cu) and to acquire an even surface for easy operation of the instrument. A total sample thickness of at least 1 mm is required to account for the maximum attenuation depth of the X-rays, equivalent to ~800 μm (Beckhoff et al., 2006). The attenuation depth differs per energy level (i.e., per element) and depends strongly on the type of material analyzed. In the case of thinner samples such as polished thin sections (~30 μm thick), materials located below the sample can affect the analysis. Therefore, a plastic sample holder and stage are used, which are composed of very light elements that cannot be measured using the μXRF technique. Samples with irregular surfaces are loaded into an entirely plastic (e.g., polypropylene) holder filled with kinetic sand and carefully placed in the same horizontal plane prior to measurement (Fig. 1B). The plastic sample holder is placed on a motorized *x*-*y*-*z* stage composed of plexiglass (polymethylmethacrylate) material. In the case of the Bruker M4 Tornado (Fig. 1C), the dimensions (length × width × height) and weight of the sample holder cannot exceed 20 cm × 16 cm × 12 cm and 5 kg, respectively.

Instrumentation

The selected proximal impactites were analyzed using a Bruker M4 Tornado benchtop micro–X-ray fluorescence instrument (Bruker Nano GmbH, Berlin, Germany) under near-vacuum conditions (20 mbar), hereafter referred to as the μXRF instrument (Fig. 1C). The mapping option, the stage precision, and the application of a vacuum represent the main benefits of this "desktop" instrument as opposed to the more common "handheld" portable-XRF (pXRF), allowing the detection of light elements up to Na (de Winter et al., 2017). The μXRF instrument uses a 30 W rhodium anode metal-ceramic X-ray tube and two 30 mm^2 silicon drift detectors (SSDs) with a resolution of 145 eV (Mn-Kα) at 300 kcps (kilocounts per second). The Rh X-ray source was operated under maximum energy settings (600 μA, 50 kV) and without the use of a filter. The X-ray beam was focused by a polycapillary lens on a spot with a diameter of 25 μm (Mo-Kα; de Winter and Claeys, 2017). A standard integration time of 1 ms per pixel and a spacing of 25 μm were employed for all μXRF mappings. In addition, μXRF spot analysis was carried out on a selection of homogenized powders, which were carefully flattened and mounted in a holder with plastic cups, using 10 points per powder and an integration time of 120 s for a defocused spot size of 200 μm.

Acquisition

Three different modes can be selected to perform the μXRF analysis with the Bruker M4 Tornado: spot, line scan, and map. The spot analysis obtains an XRF spectrum of a selected point with a spot size of 25 or 200 μm. For such a spectrum to be accurate and considered representative, it must be based on an analysis with an integration time between 60 s and 300 s (de Winter et al., 2017). For reproducibility purposes, it is also recommended to perform several random spot analyses (e.g., 10) on the same target to obtain a representative average of the measurements (de Winter et al., 2017). The line scan analysis consists of a series of—often densely spaced—spot analyses. In general, the μXRF spot and line scan analyses are useful if the user is interested in characterizing particular—often chemically homogeneous—phases or when micrometer- to millimeter-scale chemical changes throughout a phase or unit need to be accurately quantified. The relatively long measurement time on small surface areas makes the spot analysis and line scan modes unfavorable for geochemically characterizing large heterogeneous samples such as the proximal impactites in this study. A μXRF spot analysis and line scan campaign can still be useful for more in-depth geochemical studies, but only after a first characterization of the samples is carried out. Therefore, in this study, we focused on the μXRF mapping mode and do not discuss the spot and line scan analyses in more detail.

The μXRF mapping mode allows the user to cover areas that are significantly larger than those used in the spot and line scan modes, with a very short integration time per pixel (1 ms in this study). Hence, this mode is preferred as a first screening tool for (especially large) samples without characterized chemical composition. Each pixel on the acquired μXRF map has an XRF spectrum associated with that pixel. This implies that for a quantitative and representative spectrum study, an area of a complete sample or a masked-out region of interest needs to have at least 60,000 pixels to reach a total integration time of at least 60 s (de Winter et al., 2017).

Processing and Quantification

Using the Bruker M4 Esprit software, XRF spectra were converted into two types of chemical maps. First, multi-element maps were produced, which show a color assigned to each element selected, where the color of every pixel is a tone combination of the colors selected (i.e., a ratio of the selected element abundances). Second, single-element heat maps were produced, which show the relative variations of a single element on a linear red-green-blue (RGB) color (0–255) heat scale in which the highest RGB value (255) corresponds to the pixel on the map with the largest amplitude of the main (often Kα or Lα) peak of that specific element. For all maps in this study, the RGB value of a pixel was calculated by the average RGB value of the pixel itself and the eight pixels directly surrounding that pixel (a square of 3 × 3 pixels or 5625 $μm^2$). Spectra from bulk μXRF maps and regions of interest were quantified using the standardless fundamental parameters (SFP) method, resulting in volatile-free, normalized compositions in which the major elements are expressed as oxides, and the trace elements are expressed in elemental form. This standardless method uses the fundamental algorithm developed by Rousseau (Rousseau, 1984a, 1984b; Rousseau and

Bouchard, 1986; Rousseau and Boivin, 1998), which is based on the theoretical Sherman equation (Sherman, 1955) that links XRF peak intensities with the respective elemental concentrations (de Winter et al., 2017; Vansteenberge et al., 2020).

To determine the accuracy of the μXRF SFP quantification technique, 40 slabs from the IODP-ICDP Expedition 364 core and the 40 associated thin sections were analyzed by μXRF. The quantified major- and trace-element data were compared with bulk powder–based ICP-OES and ICP-MS data from the same 40 intervals but not from the exact same subsamples presented in de Graaff et al. (2019) and Déhais et al. (2019) and acquired following the methodologies outlined in Poppe et al. (2020). Those 40 homogenized powders were also analyzed by μXRF defocused (200 μm) spot analysis to compare the ICP-OES and ICP-MS data with respect to the matrix. The comparisons made for the major elements in this study were between μXRF SFP and anhydrous normalized ICP-OES data, because it is not possible to obtain loss-on-ignition data with the μXRF instrument. This direct comparison is the reason why major elements are expressed as oxides and trace elements are expressed as elements, even if μXRF also allows all elements to be expressed in elemental configuration. In addition, the SFP quantification of the bulk μXRF map of impact melt rock Pop 10 was directly compared with bulk powder XRF data from the same sample. Details about this bulk XRF technique were presented in Tagle (2004).

Digital Image Analysis

The μXRF element maps can be studied in further detail by applying digital segmentation in image analysis software to quantify modal proportions of lithological components and to determine textural characteristics (including size, shape, orientation, and sorting) of these components. This independent, quantitative data set aids in the interpretation of complex depositional mechanisms for a range of lithologies, often sedimentary. Semi-automated digital image analysis methods are commonly used to characterize heterogeneous lithologies such as proximal impactites, but most techniques are based on scans of cut and polished hand specimens or microphotographs of thin sections (Chanou et al., 2014; Pittarello and Koeberl, 2013). Here, we present a novel approach based on the geochemical composition of rock samples.

The Image Analysis module of the Zeiss (Carl Zeiss GmbH, Jena, Germany) ZEN 3.1 Pro software was used for segmenting, classifying, and quantifying different components of the Popigai impactite samples. RGB-colored μXRF multi-element maps (Fe-Si-Ca) were imported into the software and scaled based on their resolution (25 μm per pixel). Then, a classification was made of the different clast types and the groundmass present in the sample. Subsequent segmentation took place with automatic selection of phases in a designated sample frame on the μXRF map. This segmentation was based on maximum and minimum thresholds of RGB values (0–255), with a minimum particle size threshold of 0.2 mm. We also applied the option "fill holes" to exclude secondary structures inside (mainly) impact melt particles. Interactive manual segmentation was only carried out when the contrast between clast and groundmass was not high enough or when clasts consisted of multiple compositionally distinct mineral phases.

After careful digital segmentation, an extensive clast-specific data set was produced. The image analysis software exports the following output measurements for each clast: (filled) area (mm^2), convex area (mm^2), length of major and minor axes of the best-fit ellipse (mm), aspect ratio (ratio between the major and minor ellipse axis length), perimeter (mm), roundness (a value from 0 to 1 based on [4π area]/[convex perimeter]^2), sphericity (perfect circle equals 1), and convexity (convex perimeter/perimeter). It is also possible to select whether a particle at the edge of a sample touches the selected sample frame. This is useful to ensure that particles that are cut off by the outline of the sample are not incorporated in the shape parameters database because their morphologies are incomplete and hence inaccurate. However, since these particles are still part of the studied sample area, they are incorporated in the calculation of the modal abundances of classes and are also included in determining the degree of sorting using cumulative area and perimeter fractions (Chanou et al., 2014).

Subsequently, the SUM-classes export function in the ZEN 3.1 Pro software provides the total count of the clasts of one particular class, the cumulative area percentage, and average values for the particle parameters stated above. Based on these parameters, the modal abundances of the different components can be calculated together with their main particle characteristics.

RESULTS

Micro-XRF Qualitative and Semiquantitative Mapping

The direct and qualitative result from μXRF mapping is a bulk map spectrum, which represents the average chemical composition of the complete sample surface. The sample composition, the measurement conditions, the spectrometers, and the X-ray source determine the general shape of the μXRF spectrum and the presence of the elemental fluorescence peaks. The latter are always located at their typical energy levels linked to the K, L, and M lines (Beckhoff et al., 2006). Figure 2A shows the bulk map spectrum of impact breccia sample Pop C6, with the main fluorescence peaks (Kα) highlighted in bold and the secondary (and smaller) peaks (Kβ) shown in regular font. In the bulk map spectrum, the 20 Kα peaks (Na, Mg, Al, Si, P, S, Rh [from the X-ray source], K, Ca, Ti, V, Cr, Mn, Fe, Ni, Cu, Zn, Rb, Sr, and Zr) and 7 Kβ peaks (Ca, Ti, Fe, Zn, Rb, Sr, and Zr) are positively identified. For example, the Fe-Kα peak occurs at 6.404 kiloelectron volt (keV), while the Fe-Kβ peak is located at 7.058 keV. Extra caution is required when identifying elements that display peak overlap, such as the Co-Kα peak (6.930 keV) and the Fe-Kβ peak. This problem can be solved by automatic or interactive peak deconvolution in the M4 Bruker software. Three

common μXRF background spectrum characteristics are also shown in Figure 2A: the "Bremsstrahlung" and the Rayleigh and Compton peaks. The Bremsstrahlung is a wide plateau between 5 and 22 keV that is caused by the presence of backscatter without any excitation of the sample (Shackley, 2011). The Rayleigh and Compton peaks are four peaks generated due to the X-rays emitted by the Rh tube source. The Rayleigh peaks are caused by the elastic scattering of X-rays by the sample without any change in their energy (Potts and Webb, 1992) and are always located at 20.216 keV (Kα) and 22.724 keV (Kβ) for the Rh source (Fig. 2A; Vansteenberge et al., 2020). The Compton peaks are the result of inelastic scattering of X-rays, and their shift in energy compared to the Rayleigh peaks depends on the angle between the X-ray source and the spectrometer (lowest intensity at 90°). However, the scatter of the X-rays shifts the Compton peaks always toward slightly lower energies than the Rayleigh peaks (Potts and Webb, 1992).

From qualitative μXRF maps, it is possible to define regions of interest and to access the subspectra related to these areas. Figure 2B shows four subspectra of four different polygons within the Pop C6 sample, linked to chemically distinct lithological phases shown in the Fe-Si-Ca multi-element μXRF map. Note the difference in the total amount of counts for the bulk spectrum in Figure 2A and the regions of interest in Figure 2B. To allow the observation of the smallest peaks, the *y*-axis has been truncated at 100,000 counts in Figure 2B. Therefore, a comparison for Ca and Fe is not possible with the main Kα peaks, respectively at 3.692 keV and 6.404 keV, but it can be made using the secondary Kβ peaks of these two elements, respectively at 4.013 keV and 7.058 keV. The intensity comparison of the same elemental peak between several spectra provides semiquantitative information about the relative enrichment or depletion of a particular element in the regions of interest. The peak intensities show for instance that basement clast B2 is enriched in Al and Si relative to the

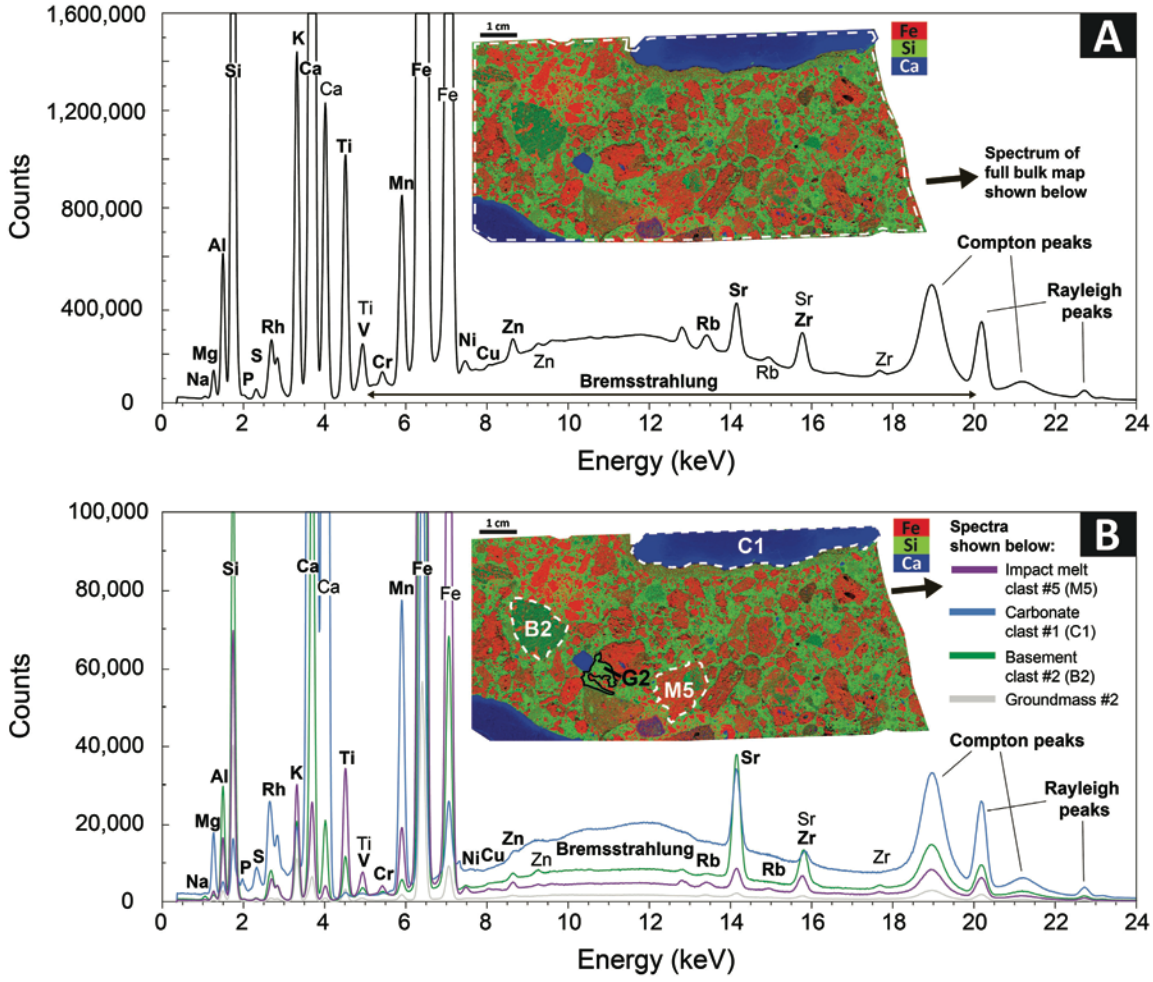

Figure 2. (A) X-ray fluorescence (XRF) spectrum of the full bulk map, and (B) spectra of four different regions of interest of the Pop C6 impact breccia sample. Note the difference in total counts between the different spectra. The polygons of the regions of interest are shown in the associated Fe-Si-Ca multi-element maps. The main fluorescence peaks (Kα) are highlighted in bold, while the secondary (and smaller) peaks (Kβ) are shown in regular font.

other regions selected. Carbonate clast C1 is enriched in Mg, P, S, Ca, and Mn relative to the other regions. Impact melt clast M5 is enriched in K, Ti, and Fe.

Figure 3 displays both types of µXRF maps for the sample Pop C6 (spectra shown in Fig. 2). The µXRF multi-element map with Fe, Si, Ca, and K directly provides clear constraints on the assemblage of different lithological components present in the sample. This impact breccia contains a range of clast sizes, from millimeters to several centimeters. Most of the greenish-yellowish clasts in the impact breccia sample Pop C6 (Fig. 1A, #5) are enriched in Fe and are likely impact melt clasts. Some clasts are enriched in Ca, and most of these do not contain any significant Fe, Si, or K, especially two large clasts at the top right (C1) and bottom left (C2) corners (Fig. 3). A few areas display black pixels, corresponding to holes in the surface and to the edges of the samples, where the X-rays were diffracted and no longer reached the detectors. The single-element heat maps of Mg, Al, Si, K, P, S, Ca, Ti, Cr, Mn, Fe, Ni, Cu, Zn, Rb, Sr, and Zr provide semiquantitative information on the distribution of these elements in Pop C6 (Fig. 3), as their relative color scale is based on RGB values from

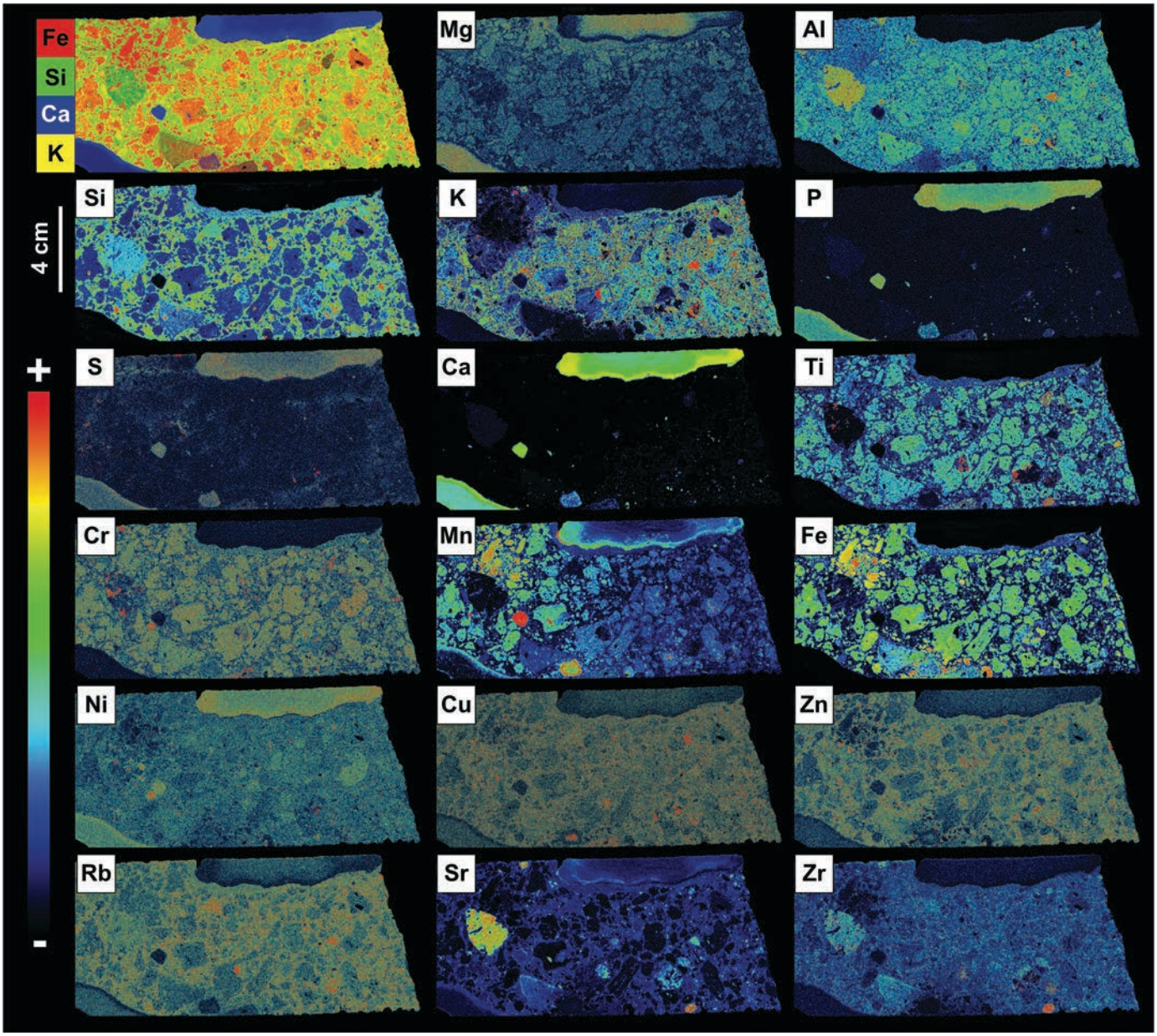

Figure 3. Pop C6 micro–X-ray fluorescence (µXRF) multi-element map with Fe, Si, Ca, and K and single-element heat maps of 17 elements (Mg, Al, Si, K, P, S, Ca, Ti, Cr, Mn, Fe, Ni, Cu, Zn, Rb, Sr, Zr). The relative red-green-blue (RGB) color scale applies to each heat map, ranging from black (RGB value of 0) to red (RGB value of 255, linked to the pixel with the highest peak amplitude of that element on the map).

0 to 255. These heat maps are correlated with the spectra shown in Figure 2. For example, clast C1 displays a spectrum with low-intensity Al, Si, Ti, Cr, Fe, Cu, Zn, Rb, and Zr peaks compared to other clasts and the groundmass (Fig. 2B) and therefore low RGB values of these elements in the respective heat maps (Fig. 3). Clast B2 shows very high counts for Al, Si, and Sr peaks relative to the other parts of the sample (Figs. 2B and 3). The comparison of fluorescence peaks in an XRF spectrum can sometimes be difficult due to low intensities; this is the case, for example, with Cu and Rb (Fig. 2B). However, the heat maps can still help to visualize that Cu and Rb are slightly more abundant in the matrix, and only a few small clasts are enriched in these elements (Fig. 3).

The RGB scale of single-element heat maps is relative for each mapped area and depends on the lowest and highest Kα peak intensities. Therefore, it is impossible to directly compare several heat maps of the same element when samples are mapped separately. To overcome this problem, several samples can be mapped together (Figs. 1B and 1C) to obtain a relative scale that is equal for the complete map area. To illustrate this approach, we mapped three impact breccia samples and three impact melt rock samples from Popigai, Ries, and Chicxulub, both individually (Fig. 4A) and all together (Fig. 4B). Between the six samples, Fe is most abundant in Pop C6, whereas the three samples Aum-01, Pols-01, and 90_1_85_87 do not contain any Fe-rich areas when compared

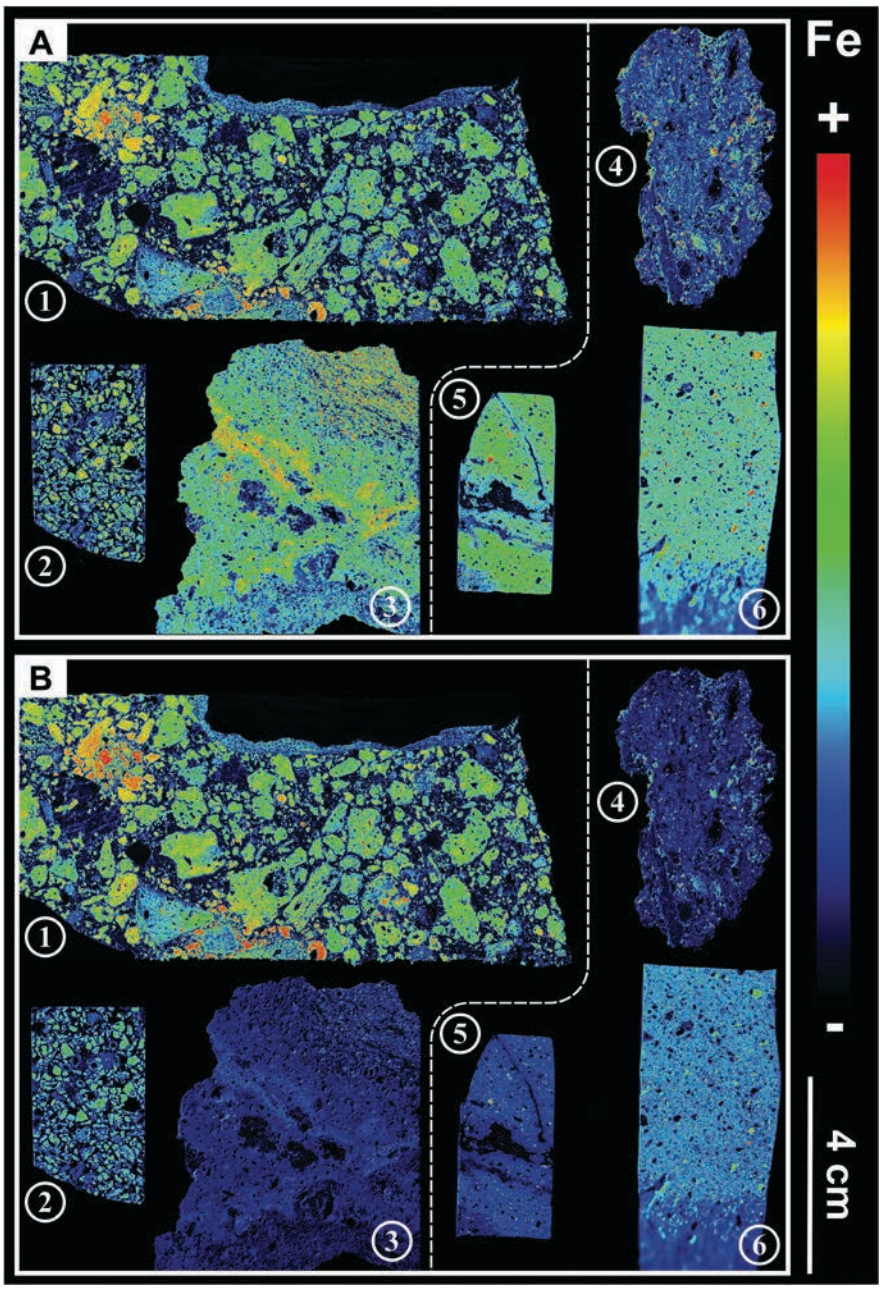

Figure 4. (A) Combined Fe heat maps of the separately analyzed samples from the Popigai, Chicxulub and Ries impact structures. (B) Single Fe heat map of the same impactite samples analyzed together. Left of the dashed line: impact breccias, with ① Pop C6, ② 54_1_64_66, and ③ Aum-01. Right of the dashed line: impact melt rocks, with ④ Pols-01, ⑤ 90_1_85_87, and ⑥ Pop 10.

to the other samples (Fig. 4B). This is clearly different when observing the Fe heat map of each sample separately (Fig. 4A).

Quantitative Image Analysis Based on µXRF Maps

Besides a qualitative approach with multi-element maps and a semiquantitative approach with single-element heat maps, the µXRF mapping technique also makes it possible to perform a quantitative image analysis based on these element maps. Figure 5 shows the workflow and results based on digital segmentation of Fe-Si-Ca µXRF maps from the two Popigai impactite samples in the Zeiss ZEN 3.1 Pro image analysis software. Impact breccia sample Pop C6 (Fig. 1A, #5; Fig. 5A) consists of a relatively equal amount (both ~40 area %) of both impact melt particles and groundmass, supplemented with ~20% of other clasts consisting of (felsic) basement clasts and carbonate clasts. Due to the high abundance of both impact melt particles and a fine-grained groundmass that appears to be clastic, this sample is classified as a matrix-supported suevite. Pop 10 (Fig. 5B) consists of 81% melt matrix and is therefore classified as a clast-poor impact melt rock (<25% clasts). The clasts in Pop 10 are subdivided into basement clasts, carbonate clasts, and Fe-rich clasts. The latter are also associated with vesicles on the sample surface (Fig. 1A, #6).

Figure 6 exhibits the particle size and shape characteristics of 1282 segmented clasts in Pop C6, subdivided into the three clast types from Figure 5A and shown both with absolute and relative frequencies. The unimodal clast-size distribution of the impact melt particle population (Fig. 6A) is dominated by a fine size range of 0.2–0.4 mm with a median of 0.37 mm. The carbonate clasts display a finer median of 0.25 mm, but they also show an additional peak at 0.6–0.7 mm. The basement clasts show a coarser and more irregular distribution with a median clast size of 0.96 mm. The roundness curve (Fig. 6B) displays a difference between more angular impact melt clasts (median of 0.43) and more rounded carbonate and basement clasts (median of 0.54 and 0.60, respectively). The aspect ratio curve (Fig. 6C) does not exhibit a clear pattern and shows for all clast groups both nonelongated and elongated clasts, although the median of the impact melt clasts is slightly higher compared to the other groups (1.72 vs. 1.45–1.53). The difference in clast morphology is more pronounced in the sphericity plot (Fig. 6D). The impact melt clasts are less spherical (median of 0.44) than the carbonate and basement clasts (median of 0.79 and 0.75, respectively).

Figure 6E shows a sorting curve for sample Pop C6 based on the relationship between the cumulative perimeter and cumulative area fractions, using all segmented clasts (n = 1351). In addition, digital segmentation was carried out on a classic, visual sorting scale commonly used in geology, following the procedure of Chanou et al. (2014). The resulting five sorting curves correspond to schematic examples of five typical degrees of sorting, ranging from very well-sorted (characterized by a slope of ~1 and a continuous linear distribution) to well-sorted (slope of 1–1.2), moderately sorted (slope of 1.2–1.7), poorly sorted (slope of 1.7–2.1), and very poorly sorted (slope of 2.1–3 and a very discontinuous distribution) samples. Based on a comparison with these five general sorting curves, sample Pop C6 can be characterized as a poorly to moderately sorted sample, as it shows a rather discontinuous distribution and a slope of ~1.7.

SFP Quantification and Comparison with Various Bulk Techniques

To determine the accuracy of the µXRF standardless fundamental parameters quantification technique, we performed a comparison study between µXRF and ICP-OES and ICP-MS data based on a wide range of Chicxulub samples (homogenized powders, thick sections, and thin sections). Figure 7 shows the µXRF mapping results on three representative samples from the IODP-ICDP Expedition 364 core, both as thick and thin sections. These samples cover the three groups of proximal impactites, with a suevite (core 54_1, 64–66 cm, 659.58 mbsf), an impact melt rock (core 90_1, 85–87 cm, 729.54 mbsf), and a shocked granitoid target rock (core 95_2, 89.5–91.5 cm, 745.78 mbsf). The bulk map spectra of the thick and thin sections of 54_1_64_66 are similar up to the Mn peak, especially for the Na, Mg, Al, Si, P, and S peaks, which cannot be distinguished from one another (Fig. 7A). The heights of the amplitude of the Kα peak of Mn and Fe are larger in the thick section compared to the thin section at 1.7 and 2.6 times, respectively. With heavier elements than Fe, the intensity of the peaks within the thin section spectrum decreases even further, resulting in barely noticeable Kα peaks for, e.g., Ni, Cu, Zn, Rb, and Zr. Similar observations were made based on the spectra of the other two core samples (90_1_85_87 and 95_2_89.5_91.5). The intensity changes around the Mn and Fe Kα peaks observed from these bulk spectra are also visible in the heat maps of these samples (Fig. 7B). The six samples were mapped together to allow the comparison of the peak amplitude of the associated elements, which is linked to the concentrations. The relative colors are comparable for the thick and thin sections of all three samples for Mg, Al, Si, and Ca maps, but not for the Fe, Ni, Rb, and Sr maps.

Figure 8 shows binary diagrams based on 40 samples from the IODP-ICDP Expedition 364 core, displaying different proximal impactites and target lithologies. The horizontal axis shows element data based on bulk powder ICP-OES and ICP-MS, whereas the vertical axis shows data based on the µXRF SFP quantification method applied on three different subsamples (200 µm spot analysis of homogenized powders, mapping of thick sections, and mapping of thin sections, respectively). The analysis of each kind of subsample has a different purpose. The 200 µm defocused spot analysis of homogenized powders, which were also used for ICP-OES and ICP-MS analysis, shows the initial error of the µXRF SFP method, as the same matrix is used in both cases. The µXRF SFP quantification of thick section maps provides information on the supplementary error added by the heterogeneity of the samples. The µXRF SFP quantification of thin section maps gives information on the additional error introduced by an insufficient thickness of the samples.

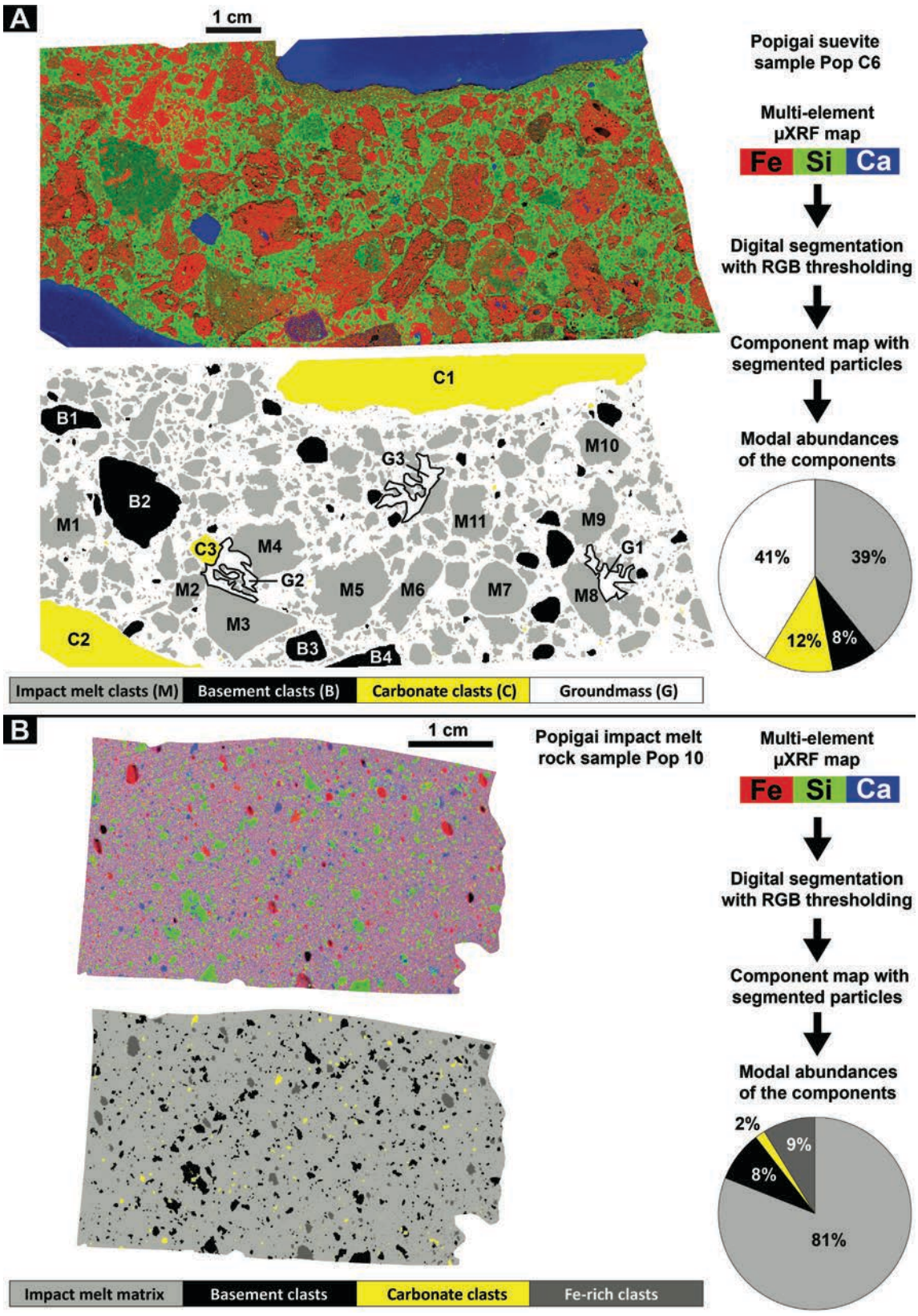

Figure 5. Results from image analysis derived from digital segmentation based on multi-element Fe-Si-Ca micro–X-ray fluorescence (µXRF) maps from (A) Popigai suevite sample Pop C6 and (B) impact melt rock sample Pop 10. Schematic workflow is indicated for both samples, together with the corresponding component map showing segmented particles and the area fraction (%) of the four different lithological/geochemical groups per sample. RGB—red-green-blue color scale.

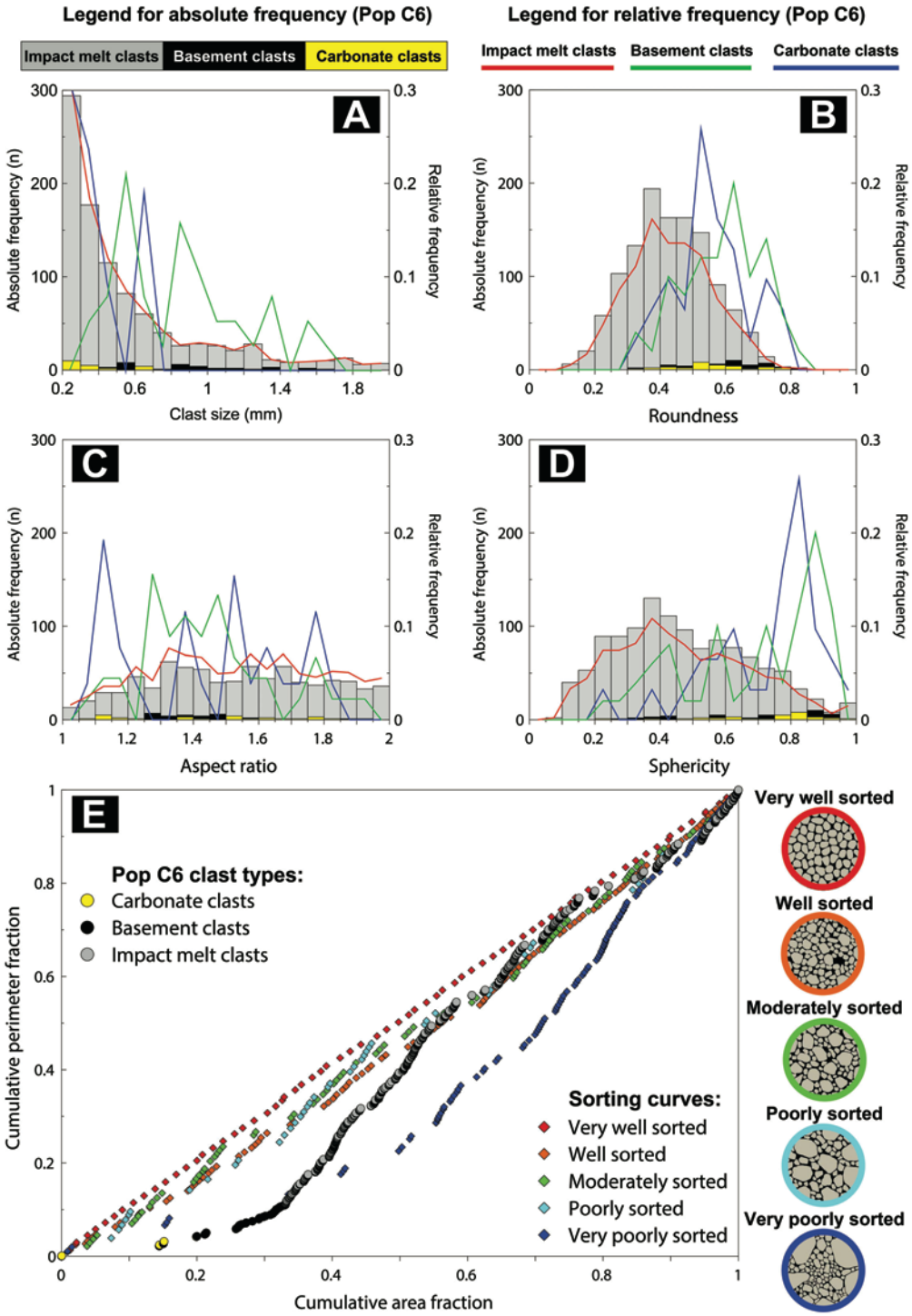

Figure 6. Overview of particle size, shape, and sorting parameters derived from the digital segmentation of suevite sample Pop C6. (A–D) Histograms show the distributions of three clast groups within Pop C6, all expressed on an absolute frequency scale and a relative frequency scale per clast group: impact melt particles (n = 1201, shown as gray bars in the absolute frequency scale and as red lines in the relative frequency scale), basement clasts (n = 50, black bars and green lines), and carbonate clasts (n = 31, yellow bars and blue lines). (A) Clast size is based on the length of the major axis (in mm) of the best-fitting ellipse around each segmented clast. (B) Roundness for each clast is a unitless number between 0 and 1 and is calculated based on (4π area)/(convex perimeter)^2. (C) Aspect ratio indicates the elongation of every clast and is calculated by dividing the major axis and minor axis of the best-fit ellipse. (D) Sphericity is a unitless number between 0 and 1 ([4π area]/[Crofton perimeter]^2), in which 1 indicates a perfect circle. (E) Sorting plot based on Chanou et al. (2014) displaying the cumulative area fraction vs. the cumulative perimeter fraction for all Pop C6 clasts (n = 1351: 1255 impact melt clasts, 57 basement clasts, and 39 carbonate clasts). As a comparison, five sorting curves (from very well sorted to very poorly sorted) are shown based on digital segmentation of schematic visualizations of a typical sorting scale used in geology. Very well-sorted samples display (in red diamonds) a slope of ~1 and are characterized by a continuous linear distribution, whereas very poorly sorted samples (in blue diamonds) show a discontinuous pattern and can reach slopes larger than ~2.5.

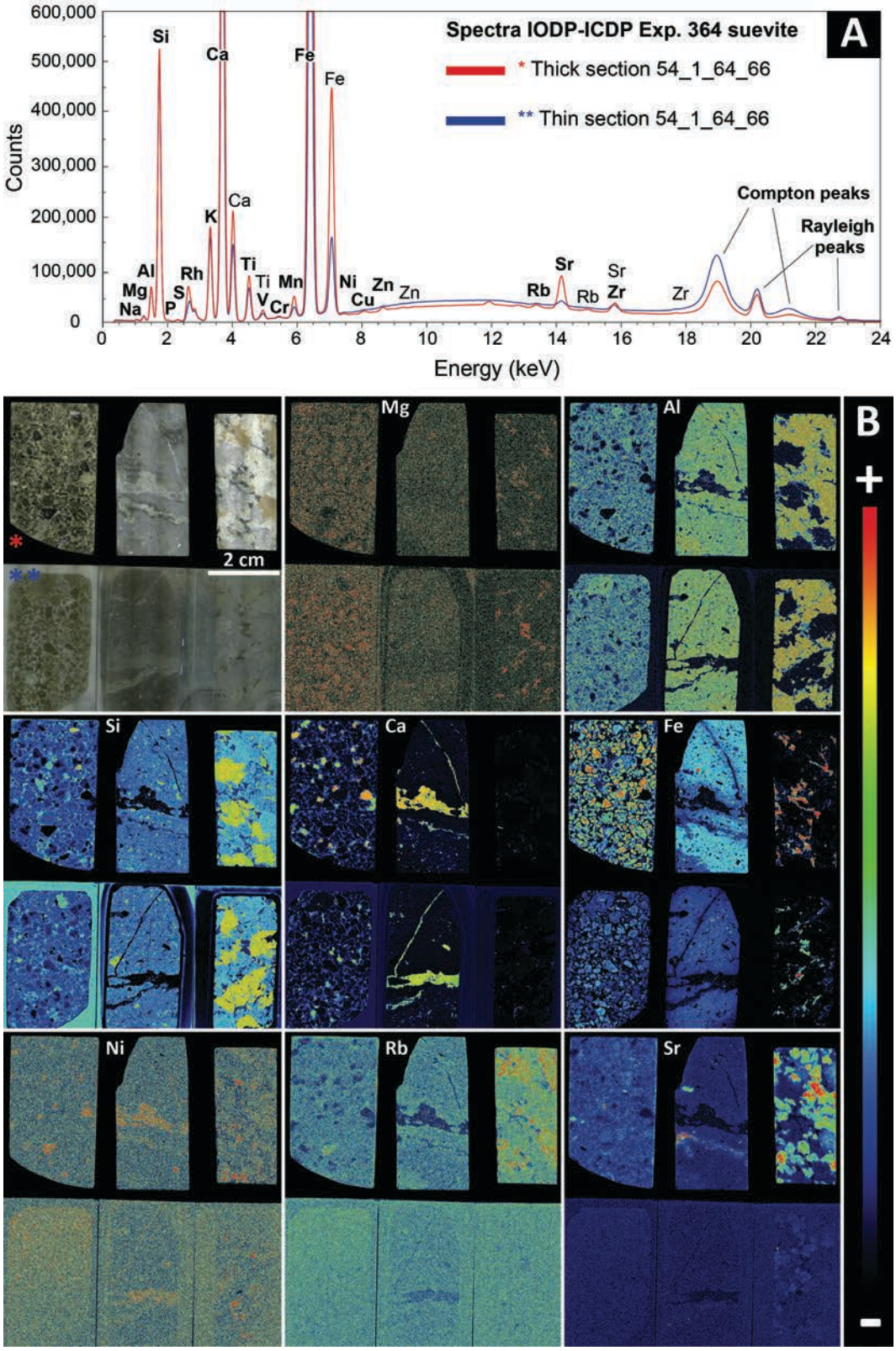

Figure 7. (A) X-ray fluorescence (XRF) spectra of the thick and thin sections of International Ocean Discovery Program–International Continental Drilling Project (IODP-ICDP) Expedition 364 suevite sample 54_1_64_66. (B) Scans and single-element micro–X-ray fluorescence (μXRF) heat maps (Mg, Al, Si, Ca, Fe, Ni, Rb, Sr) of three IODP-ICDP Expedition 364 samples: a suevite sample 54_1_64_66 (left), an impact melt rock 90_1_85_87 (center), and a granitoid target rock 95_2_89.5_91.5 (right) (thick sections on the top row and associated thin sections on the bottom row).

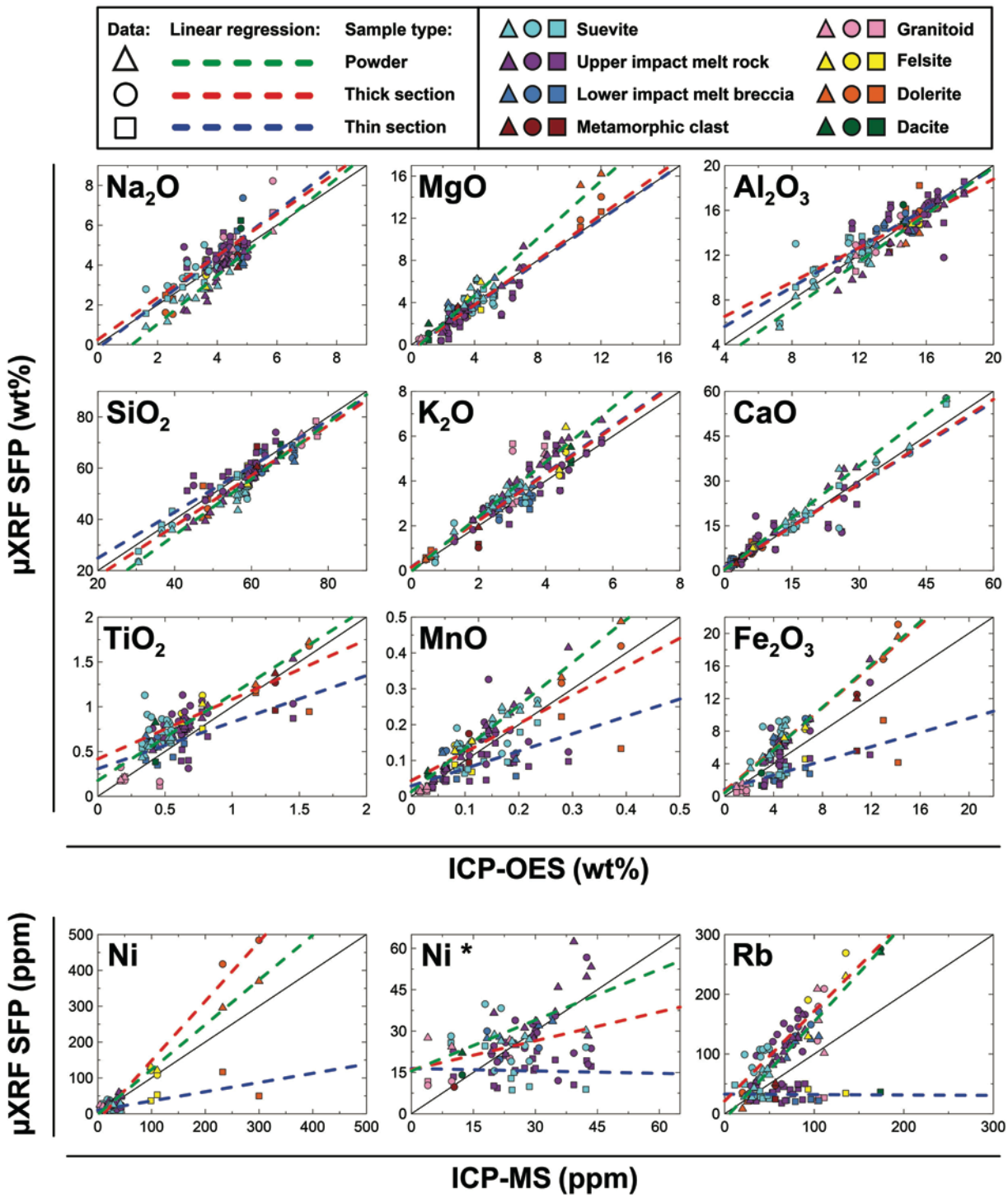

Figure 8. Binary diagrams of the micro–X-ray fluorescence (µXRF) standardless fundamental parameters (SFP) method quantification results (ordinate; based on homogenized powders, thick sections and thin sections) vs. corresponding bulk major- and trace-element data (abscissa; based on inductively coupled plasma–optical emission spectrometry [ICP-OES] and inductively coupled plasma–mass spectrometry [ICP-MS]) of the same 40 Chicxulub International Ocean Discovery Program–International Continental Drilling Project (IODP-ICDP) Expedition 364 core samples for nine major elements and two trace elements. Identical results fall on a slope of 1, as indicated by the black straight line. Corresponding slopes, intercepts, and R^2 values are displayed in Table 1. Data are shown in Tables A1 (homogenized powders, 200 µm µXRF spot analysis), A2 (µXRF mapping of thick sections), and A3 (µXRF mapping of thin sections). Graph Ni* is a second Ni graph without the data points of the dolerite and felsite samples to visualize the ability of µXRF to quantify low Ni concentrations.

The major elements, expressed as oxides Na_2O, MgO, Al_2O_3, SiO_2, K_2O, CaO, TiO_2, MnO, and Fe_2O_3, and the trace elements Ni and Rb are shown to illustrate the comparison between the different techniques (Fig. 8). The slope, intercept, and R^2 value of the linear regressions derived from the graphs shown in Figure 8 are reported in Table 1, and the μXRF SFP quantification data are reported in Table A1 (homogenized powders with 200 μm spot analysis), Table A2 (mapping of thick sections), and Table A3 (mapping of thin sections). For all major elements in the homogenized powder analysis, the slope of the linear regression is close to 1 (except for MgO and Fe_2O_3, which are 1.36 and 1.31, respectively) and associated with an excellent $R^2 > 0.9$ (except for Na_2O, which has $R^2 = 0.88$). This indicates that the μXRF SFP quantification on homogenized powders and the ICP-OES technique are in very good agreement for all the major elements.

For both thick and thin sections, from Na_2O to CaO (six major elements out of nine), the slope of the linear regression is close to 1 and associated with good $R^2 > 0.77$ (except for Na_2O and Al_2O_3 in thick sections, with $R^2 = 0.59$ and $R^2 = 0.66$, respectively). This indicates that the μXRF SFP quantification of thick and thin sections and the ICP-OES technique are in reasonable to good agreement for those elements. The slope and R^2 values for TiO_2 are similar for thin and thick sections but are not as good as for the other major elements described above. For MnO and Fe_2O_3, the thick sections show slope and R^2 values close to the relatively high values of Na_2O to CaO, in contrast to the thin sections, which yield lower values with slopes of 0.44–0.49 and R^2 values of 0.42–0.56. This change at MnO and Fe_2O_3 is also visible in Figure 8, in which the blue trend line of the thin sections starts to deviate from the other two trend lines. Both the slope and the R^2 values for the thin sections decrease drastically for all trace elements heavier than Fe_2O_3 (all slopes < 0.26, all $R^2 < 0.42$), as can be seen in the bivariate plot for Ni and Rb.

The case of Ni is particularly interesting, because at first the correlation between μXRF SFP quantification and ICP-MS data seems to be excellent for homogenized powders and thick sections (slope of 1.25 and 1.66, R^2 of 0.98 and 0.96, respectively). However, these values are only valid when all samples are taken into account (graph "Ni" in Fig. 8). Most of the samples fall within a low-concentration range (10–45 ppm). The only outliers are the two felsite samples (~100 ppm of Ni) and the two dolerite samples (230–300 ppm of Ni), which control the good correlation for the nickel. To visualize the ability of μXRF to quantify low Ni concentration, a second Ni graph without the data points of dolerite and felsite samples is shown in Figure 8 (graph "Ni*"), and the associated linear regression parameters are reported in Table 1. If only the two dolerite samples are removed, the slope and R^2 values are still in good agreement with ICP-MS data (slope of ~0.9–1.1 and R^2 of 0.75–0.87) for both homogenized powders and thick sections. If the two dolerite and the two felsite samples are removed, the linear regression parameters show a bad correlation with ICP-MS data (slope of ~0.35–0.61 and R^2 of 0.14–0.40). All these observations indicate that the μXRF SFP quantification is accurate for homogenized powders for all major elements and most trace elements and is relatively accurate for thick sections up to Fe_2O_3 and for thin sections up to CaO.

To visualize and further quantify the trends observed in Figures 7 and 8, the concentrations determined by the μXRF SFP technique were compared to those derived from bulk ICP-OES and ICP-MS data. Figure 9 displays a box-whisker plot showing the deviation of the μXRF SFP quantification from the bulk ICP-OES and ICP-MS results for the different major (as oxides) and trace elements. The median deviations and interquartile ranges visualized in Figure 9 are also summarized in Table 1. The trend is similar between homogenized powders (Fig. 9A) and thick sections (Fig. 9B), although the homogenized powders display for most elements a smaller interquartile range and whisker range. The method is relatively accurate from Na_2O to MnO. From Fe_2O_3 to Zr, the deviation from the bulk data increases (1) in the positive direction for homogenized powders (Fig. 9A) and for thick sections (Fig. 9B) and (2) in the negative direction for thin sections (Fig. 9C). Also, the precision decreases with heavier elements, visible as an increase in the size of the envelopes, both in the interquartile range and the whisker range. From Fe_2O_3 toward heavier elements, the technique tends to overestimate the concentrations in the homogenized powders and the thick sections, and to underestimate the concentrations in the thin sections.

The impact melt rock Pop 10 has been analyzed by bulk powder XRF (Tagle, 2004), and, therefore, the μXRF SFP quantification of this sample can be compared to this other bulk technique. The results are shown in Table 2. The concentrations obtained with the μXRF technique (on a homogenized powder and a thick section) are close to the values published by Tagle (2004). The thick sections show a deviation of less than 10% for the major elements (expressed as oxides) Na_2O, Al_2O_3, SiO_2, CaO, TiO_2, MnO, and Fe_2O_3. Larger deviations are observed for K_2O, MgO, P_2O_5, and SO_3. For the two first major elements, this difference is likely explained by comparison between different subsamples of the same sample (Tagle, 2004; this study). Therefore, even if Pop 10 had been determined to be a clast-poor impact melt rock (Fig. 5B), a variation in the presence of clasts from the target lithologies (Vishnevsky and Montanari, 1999) in the sample can explain the observed difference in MgO, K_2O, and SiO_2 values. In the case of P_2O_5 and SO_3, the concentrations are very low (<0.1 wt%), so the values are below the limit of quantification. As already shown with the analysis of the Expedition 364 samples (Fig. 9B) and for the bulk XRF comparison, the μXRF SFP quantification overestimates trace-element concentrations, except in the case of Y and Ba. However, the determined Ni, Cu, and Zr results exhibit a deviation of <15% compared to the bulk XRF values. Regarding the Ni quantification, it is important to notice that the Ni concentration of Pop 10 (>120 ppm) is higher than most samples from the Chicxulub IODP-ICDP Expedition 364 drill core used in this study, which indicates that μXRF SFP quantification of these high levels of Ni concentrations is meaningful. This confirms the potential of μXRF to track meteoritical components, which are frequently linked to Ni enrichment in impactites (e.g., Lambert, 1975; Grieve et al., 1981; Goderis et

TABLE 1. LINEAR REGRESSION AND ACCURACY PARAMETERS OF THE MICRO–X-RAY FLUORESCENCE (μXRF) STANDARDLESS FUNDAMENTAL PARAMETERS (SFP) QUANTIFICATION OF CHICXULUB IMPACTITE SAMPLES

Elements	Homogenized powders, 200 μm spot analysis					Thick section map					Thin section map				
	Slope*	Intercept*	R^2*	Median deviation† (%)	Interquartile range† (%)	Slope*	Intercept*	R^2*	Median deviation† (%)	Interquartile range† (%)	Slope*	Intercept*	R^2*	Median deviation† (%)	Interquartile range† (%)
Major (wt%)															
Na_2O	1.22	–1.39	0.88	–15.5	16.3	1.05	0.26	0.59	9.5	26.2	1.15	–0.18	0.86	9.6	14.0
MgO	1.36	–0.81	0.93	7.5	32.9	1.07	–0.48	0.87	–6.8	29.6	1.03	–0.37	0.87	–12.3	29.6
Al_2O_3	1.05	–1.19	0.92	–2.3	9.9	0.77	3.47	0.66	0.9	11.8	0.88	2.12	0.79	2.8	11.7
SiO_2	1.10	–10.12	0.95	–6.9	7.5	0.98	–1.77	0.87	–5.6	7.2	0.90	6.99	0.85	2.0	9.7
K_2O	1.22	–0.04	0.95	22.2	12.0	1.04	0.15	0.80	7.0	21.3	1.05	0.16	0.77	9.2	26.9
CaO	1.16	0.26	0.99	17.9	11.0	0.95	0.55	0.88	6.5	23.7	0.92	1.22	0.92	15.3	48.3
TiO_2	0.96	0.18	0.93	25.1	16.7	0.67	0.42	0.49	41.9	43.4	0.52	0.31	0.50	12.5	36.0
MnO	1.20	0.01	0.92	29.3	22.4	0.80	0.04	0.58	22.1	50.0	0.49	0.03	0.42	–26.2	32.7
Fe_2O_3	1.31	0.44	0.96	39.3	12.3	1.27	0.68	0.83	36.5	37.0	0.44	0.87	0.56	–41.5	24.0
Trace (ppm)															
Cr	0.96	21.94	0.91	34.3	57.1	1.21	22.62	0.85	78.6	119.3	0.54	21.33	0.67	17.2	91.8
Ni§	1.25	–1.49	0.98	15.2	28.5	1.66	–17.86	0.96	2.4	39.5	0.26	10.03	0.63	–46.6	29.2
Ni (–d)#	1.11	2.56	0.87	14.2	31.5	0.94	1.93	0.75	1.2	36.9	0.31	8.09	0.57	–45.1	29.8
Ni (–d&f)**	0.61	15.55	0.40	14.2	31.5	0.35	16.02	0.14	1.2	38.4	–0.03	16.43	0.00	–43.9	30.9
Cu	1.27	0.48	0.80	19.5	53.6	0.63	25.09	0.25	31.6	100.8	0.01	18.22	0.00	–54.8	44.1
Zn	1.03	75.61	0.61	166.2	139.7	0.11	107.62	0.03	118.7	142.0	–0.02	41.86	0.01	–14.5	79.7
Ga	0.76	10.67	0.39	23.4	61.9	0.05	31.18	0.00	67.2	114.5	–0.25	24.37	0.18	–3.6	105.8
Rb	1.63	–8.88	0.89	55.5	25.3	1.50	21.42	0.77	88.1	66.0	–0.01	32.82	0.00	–40.4	40.3
Sr	2.04	–45.25	0.95	87.7	27.3	2.64	–135.89	0.76	122.1	57.1	0.26	79.50	0.42	–54.6	13.6
Y	1.38	–2.39	0.85	24.6	21.7	1.38	6.34	0.67	74.2	49.7	N.A.	N.A.	N.A.	N.A.	N.A.
Zr	1.50	9.02	0.88	55.2	28.5	1.38	51.62	0.46	89.3	54.1	–0.42	185.92	0.09	26.7	128.1

Note: Table shows linear regression parameters from the graphs shown in Figure 8 together with median deviation and interquartile range for each element from Figure 9. Data are shown for homogenized powders, thick sections, and thin sections, which were derived from 40 impactite drill core samples collected during the Chicxulub International Ocean Discovery Program–International Continental Drilling Project (IODP-ICDP) Expedition 364. N.A.—not applicable (data below detection limits).

*Linear regression parameters from the graphs in Figure 8.

†Box-and-whisker plot parameters from Figure 9.

§Ni = parameters for nickel acquired with all data. Correspond to graph "Ni" in Figure 8.

#Ni (–d) = parameters for nickel acquired with all data minus the two dolerite samples.

**Ni (–d&f) = parameters for nickel acquired with all data minus the two dolerite and the two felsite samples. This corresponds to graph "Ni*" in Figure 8.

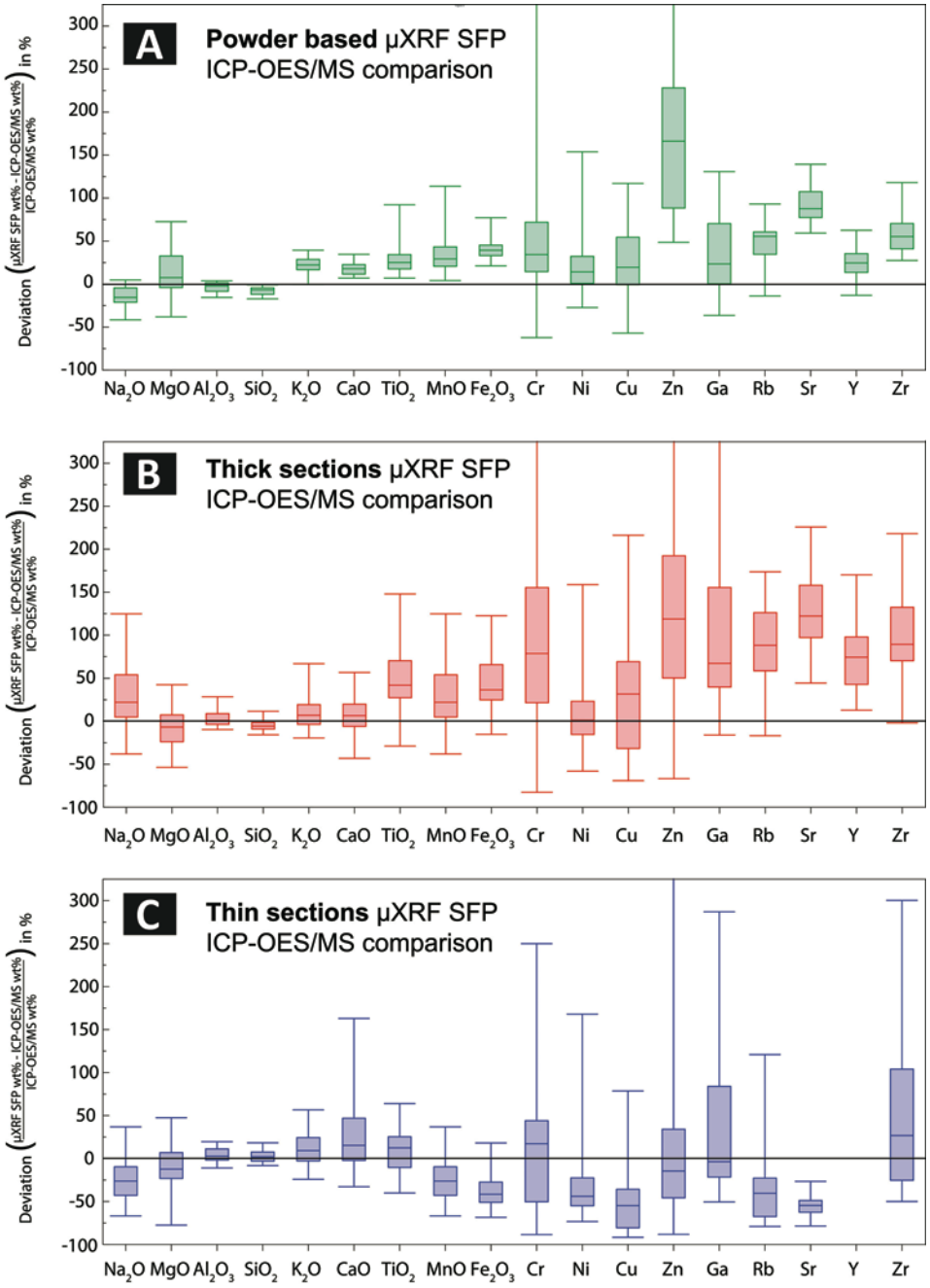

Figure 9. (A–C) Box-and-whisker plots displaying the deviation of a series of major and trace elements when comparing bulk powder data from inductively coupled plasma–optical emission spectrometry/mass spectrometry (ICP-OES/MS), with results derived from a standardless fundamental parameters (SFP) quantification of micro–X-ray fluorescence (μXRF) defocused (200 μm) spot analysis of homogenized powders (A), μXRF maps of thick sections (B), and μXRF maps of thin sections (C) from 40 Chicxulub International Ocean Discovery Program–International Continental Drilling Project (IODP-ICDP) Expedition 364 core samples. The box size, i.e., interquartile range, represents 50% of the data. The line within the box corresponds to the median, and the whiskers represent 90% of the data. The median and interquartile ranges for these elements are also shown in Table 1.

al., 2012). Due to peak deconvolution issues, the Co and V values cannot be verified, as they are biased by the overlapping Fe and Ti peaks, respectively.

DISCUSSION

Optimization of μXRF Mapping

The first major advantages of the μXRF mapping technique are the fast and easy sample preparation and the nondestructive nature of the analysis. These make μXRF a powerful tool to geochemically characterize proximal impactites, especially in the case of complex or precious samples such as impact breccias and drill core samples. When using an integration time of 1 ms per pixel with a spacing of 25 μm, the instrument takes approximately 1 h to map an area as wide as a standard geological thin section (~4 × 2 cm, ~8 cm^2) and roughly 1 d for a map covering the maximum sample size (~16 × 20 cm, ~320 cm^2). In case of time constraints for the completion of a map, the duration of the analysis can be shortened by increasing the spacing. This leads

TABLE 2. COMPARISON OF MICRO–X-RAY FLUORESCENCE (μXRF) STANDARDLESS FUNDAMENTAL PARAMETERS (SFP) QUANTIFICATION WITH BULK POWDER XRF ANALYSIS (TAGLE, 2004) ON POPIGAI IMPACT MELT ROCK SAMPLE Pop 10

Elements	Bulk powder XRF*	μXRF SFP results		Deviation from bulk powder XRF (%)	
		Homogenized powder, 200 μm spot analysis†	Thick section mapping	Homogenized powder, 200 μm spot analysis†	Thick section mapping
Major (wt%)					
Na_2O	2.24	1.57	2.38	–29.9	6.2
MgO	3.49	2.58	2.39	–26.1	–31.4
Al_2O_3	15.86	15.02	15.11	–5.3	–4.7
SiO_2	63.62	64.01	65.89	0.6	3.6
P_2O_5	0.09	B.D.L.	B.D.L.	N.A.	N.A.
SO_3	0.10	B.D.L.	B.D.L.	N.A.	N.A.
K_2O	3.02	3.45	2.46	14.4	–18.5
CaO	3.45	3.47	3.22	0.8	–6.4
TiO_2	0.78	0.87	0.71	11.1	–9.6
MnO	0.07	0.08	0.07	16.6	6.7
Fe_2O_3	7.07	8.95	7.76	26.5	9.8
Trace (ppm)					
V	116	N.A.	N.A.	N.A.	N.A.
Cr	104	175	249	68.9	139.4
Co	28	N.A.	N.A.	N.A.	N.A.
Ni	127	170	146	33.8	14.9
Cu	<30	30	32	1.0	6.2
Zn	86	115	110	33.8	27.0
Rb	91	115	112	25.6	22.9
Sr	255	384	347	50.4	35.7
Y	35	43	26	23.0	–25.6
Zr	280	381	306	36.0	9.2
Ba	932	473	660	–49.2	–29.2
Pb	<15	9	B.D.L.	–42.4	N.A.

Note: B.D.L.—below detection limit; N.A.—not applicable.
*Average value (n = 2) from Tagle (2004).
†Average value (n = 10).

to a loss in spatial resolution, but in the case of large samples (>100 cm^2 surface area), smaller regions of interest can efficiently be identified and eventually rescanned later at a higher resolution. The μXRF technique is also competitively priced, as no consumables are involved, and the cost per measurement remains consequently relatively low.

However, a few issues must be kept in mind when interpreting μXRF maps. A commonly encountered problem is linked to focusing, as only one focus plane can be selected while performing μXRF mapping. When a sample is not completely flat or displays edges and holes, the excitation of primary X-rays and the subsequent detection of secondary X-rays are inhibited. This can lead to blurred areas on the μXRF maps, as can be seen for example in the bottom part of Pop 10, which is lower in elevation than the focal plane (Fig. 4, #6). Another problem is the presence of exogenous or preparatory materials such as tape, glue residue, or notes on the samples, which affect some element maps. This was observed for the label written at the bottom of the IODP-ICDP Expedition 364 thin sections, because the ink was enriched in S and Ti. Therefore, a careful selection of the mapping area is required to avoid any quantification problems for μXRF maps. It is also important to note that even if the μXRF is a surface technique, the X-rays penetrate the samples by several hundreds of micrometers (Beckhoff et al., 2006). This means that the analysis incorporates (potentially enriched) phases that are not exposed at the surface and observable by the naked eye.

Multi-element μXRF maps are useful to directly identify multiple mineral or lithological phases and to classify complex samples such as impact breccias, which often contain a wide range of different lithologies (Figs. 2 and 3). Theoretically, it is possible to create multi-element maps with as many elements as possible. However, a different color needs to be assigned to each element selected in the map. Due to the complementarity of colors, the most effective multi-element maps are those combining 2–4 elements.

In contrast, single-element heat maps visualize the elemental distribution of a single selected element (Figs. 3 and 4). Each map has its own linear RGB color scale (0–255) based on the lowest and highest peak amplitude for each element selected within the sample. These peak amplitudes are linked to concentrations, but other factors like matrix effects and element-specific characteristics such as fluorescence yield also play a significant role in peak intensity (Beckhoff et al., 2006). Because of the relative scaling, element distribution maps of individually scanned samples cannot be compared in terms of absolute concentrations. Heat maps can only be compared if all the samples are mapped together (Figs. 4B and 7B) or if the sample composition is well constrained by other techniques such as bulk XRF, ICP-OES and ICP-MS, EMPA, or LA-ICP-MS.

μXRF-Based Image Analysis: Interpretations and Implications

Digital image analysis of semi-automated segmentation based on μXRF maps of proximal impactites is successful in producing quantitative modal abundances (Fig. 5) as well as an extensive data set of particle parameters (Fig. 6). As the segmentation in this method is based on the geochemical composition, clast type misidentifications on sample surfaces due to visual aspects such as color—potentially influenced by postimpact alteration—are limited.

For instance, in Pop C6 (Fig. 1A, #5), a large gray clast is visible in the upper right (C1) while a medium-large brown clast is found in the lower left (C2). These clasts are visually distinct, but they have a similar chemical composition based on the μXRF maps (Fig. 3) and are therefore classified as clasts from a carbonate target lithology. Pop C6 is classified as a matrix-supported suevite (Fig. 5A) based on a groundmass that appears to be clastic, a clast/matrix ratio of 60% versus 40%, and a dominance of impact melt particles (~40%). The impact melt particles in Pop C6 are more angular and less spherical than the carbonate and basement clasts (Figs. 6A–6D). Pop C6 does not display clear bedding or a preferred orientation of clasts, and it is characterized as a poorly to moderately sorted suevite (Fig. 6E) based on the cumulative perimeter and area fractions of the entire clast population.

This quantitative information sheds light on the physico-mechanical processes of formation, transport, and emplacement of this Popigai suevite. The impact melt particles in Pop C6 are dominated by angular, green/gray porous clasts (Fig. 1A) that are rich in Fe and do not exhibit large numbers of other mineral or lithic clasts within them (Figs. 3 and 5A). These are interpreted as remnants of quenched melt, resulting in glassy or vitric melt particles, which are easily weathered out (hence leading to a porous texture). Another type of impact melt particle exists, illustrated by clasts M3 and M7 (Fig. 5A), as this type is characterized by higher SiO_2 and lower Fe_2O_3 contents compared to the vitric melt particles (based on μXRF SFP quantifications of these regions of interest, as shown in Table A4). The clasts from this second type of impact melt are also angular in shape and characterized by entrained mineral and lithic clasts from the felsic basement. These could represent brecciated parts from the central melt sheet transported into the suevite unit. Overall, Pop C6 fits the description of lithovitroclastic suevites with predominantly greenish melt particles and a small fraction of both crystalline and sedimentary clasts. These suevites are described from the lower part of the upper member of the Popigai crater fill sequence (Naumov, 2002; Raikhlin, 1996; Masaitis, 2003). This suevite is interpreted to have been emplaced by a combination of base surge and settling from the collapsed hot vertical part of the explosion cloud without significant water-melt interaction (Masaitis et al., 2018). Pop 10 consists of 19% clasts and is therefore classified as a clast-poor impact melt rock, which fits the literature description of the high-temperature impact melt rock or T2 melt rock observed in the Popigai impact structure (summarized by Whitehead et al., 2002).

In this study, we used Fe-Si-Ca multi-element maps of thick sections as a basis for the digital segmentation, but single-element heat maps of polished thin sections can also be used. Figure 7 indicates that the intensities of the RGB-colored heat maps do not show clear differences in elements ranging from Mg to Ca. The Fe heat maps display a decrease in intensities for the thin sections, but due to the large abundance of Fe in impactites, the main features (e.g., melt particles in suevites) can still be recognized and are therefore useful for the segmentation. The benefit of using μXRF maps on thin sections is that petrographic features such as shock metamorphism, in particular, mineral phases and the nature of a clast matrix or a groundmass (e.g., clastic, vitric, or microcrystalline microtextures), can directly be compared and studied. This allows for the segmentation of clasts not only based on chemical aspects, but also based on mineralogical features. Overall, the incorporation of geochemical micrometer-scale distribution maps as a basis for semi-automated digital segmentation unlocks a broad range of applications in geosciences. This technique produces quantitative textural data sets combined with geochemical information, in both a systematic and a time-efficient manner.

Implications and Applications of SFP μXRF Quantification

Differences between Thick and Thin Section Quantifications

The μXRF SFP quantification on thick and thin sections exhibits a clear trend (Figs. 7–9). Our results indicate that the technique quantifies all elements identified in the spectra for the thick sections, thereby showing comparable results to the homogenized powders but with a lower precision in general, but especially for trace elements (visible as larger interquartile and box-whisker ranges in Fig. 9B compared to Fig. 9A). From Na to Mn, the SFP quantification for the thick sections displays good accuracy (slope ~1 and deviation <10% from Na_2O to CaO) compared to the bulk ICP-OES data (Table 1). For Fe and heavier elements, the μXRF method tends to consistently overestimate the concentrations, as indicated by the high positive deviation of

several tens of percent (Figs. 8 and 9B; Table 1). As mentioned in the Results section, nickel is an important element to track meteoritical components in impactites (Goderis et al., 2012, 2013a). Our results for low-Ni-concentration (10–45 ppm) Chicxulub IODP-ICDP Expedition 364 samples exhibit the difficulty to properly quantify such low concentrations for this trace element (Fig. 8; Table 1). However, for homogenized powders and thick sections, higher Ni concentrations (50–300 ppm) are slightly overestimated (dolerite and felsite samples in Fig. 8; Pop 10 in Table 2). As many types of impactor are enriched in Ni (Tagle and Berlin, 2008) compared to most of the terrestrial target rocks, this implies that many impactites are Ni-rich. Therefore, the μXRF SFP quantification of Ni-rich samples (>50 ppm) is still relevant to provide first clues about the Ni concentration for further analysis. Regarding the thin section analysis, our results indicate that the technique also provides accurate data for elements ranging from Na to Ti (deviation <15%). However, for Mn and heavier elements, the SFP quantification underestimates the concentrations (deviation highly negative by several tens of percent) or is not consistent with the bulk ICP-OES and ICP-MS data (slopes and R^2 close to 0; Figs. 8 and 9C; Table 1).

As the thick and associated thin sections represent two different surfaces from the same core intervals, the main difference between the two sample types is their respective thickness, which is ~30 μm for thin sections and >1 mm for thick sections. X-rays penetrate the sample surfaces, and therefore the thickness of the sample and the composition of the nonvisible deeper phases influence the μXRF map results. Moreover, the attenuation depth of X-rays is different for each element and differs strongly depending on the type of geological material (Beckhoff et al., 2006). To explain the differences observed in Figures 7–9, the attenuation depths for a range of different geological materials were calculated (see Fig. A1 and Table A5 in the Appendix; Henke et al., 1993). The selection of these geological materials was based on the most important mineral groups within the IODP-ICDP Expedition 364 core determined by bulk powder X-ray diffraction (Morgan et al., 2017). In total, nine mineral groups were selected: calcite, quartz, muscovite, albite, anorthite, orthoclase, analcime, saponite, and clinochlore. Based on the raw attenuation depths and corresponding X-ray energies, the intercepts for each Kα peak of the elements from Na to Zr were calculated for the different mineral groups (see Table A5 and Fig. A1 in the Appendix). These intercepts correspond to the depth (in μm) that the X-rays need to reach in order for the sample to receive a full excitation and response. Considering a thin section thickness of 30 μm, the calculated intercepts indicate that for most of the selected materials, the μXRF detectors no longer receive a full response from the samples for the energies corresponding to the Cr-Kα and Mn-Kα peaks (5.4–5.9 keV). As the samples analyzed from the IODP-ICDP Expedition 364 core represent a mixture of the selected mineral groups, we conclude that SFP quantifications of elements from Na to Ti are applicable for μXRF maps of thin sections. Every element heavier than Mn or Fe cannot properly be analyzed because the intercepts of the Kα energies with the attenuation depths are larger than 30 μm. Detection of Fe based on μXRF mapping of thin sections remains possible, as shown in Figure 7B, despite an incomplete response due to a deeper calculated intercept. This observation is linked to the generally high abundance of Fe in impactite samples and the high fluorescence yield of Fe (Beckhoff et al., 2006). Therefore, Fe heat maps of thin sections can still be used to characterize proximal impactites, albeit not quantitatively. Another observation from these intercept calculations is that the analysis of thick sections should be carried out on samples with a thickness of at least ~1 mm to ensure correct μXRF quantifications of heavy elements such as Sr and Zr.

The advantage of μXRF mapping on thin sections is the possibility to directly compare the geochemical results with optical or scanning electron microscope images, or to use μXRF maps in combination with analytical techniques such as EMPA or LA-ICP-MS. However, a direct comparison of a thin section with a μXRF map of the corresponding counterpart slab often remains challenging due to the incomplete match between the two pieces as a result of the thin section preparation.

Popigai Case Study

Figures 8 and 9 and Tables 1 and 2 demonstrate that the μXRF SFP quantification on thick sections leads to results that are comparable to both bulk ICP-OES/ICP-MS and bulk XRF for major elements (expressed as oxides, from Na_2O to Fe_2O_3). Therefore, we applied this quantification technique to characterize the two Popigai impactite samples, using spectra of both the bulk maps (Pop C6 and Pop 10) and the regions of interests for Pop C6. The latter are shown as annotated components (e.g., C1, B2, G3, M4, etc.) in Figure 5A. The geochemical results are compared to literature data in two ternary diagrams shown in Figure 10. Data for those ternary diagrams can be found in Table A4 in the Appendix. The μXRF bulk values of both samples fall within the range of concentrations determined by literature (Rabkin, 1959; Lutz, 1985; Vishnevsky and Montanari, 1999; Whitehead et al., 2002; Kettrup et al., 2003; Tagle, 2004; Tagle and Claeys, 2005) for their respective lithological unit (Fig. 10A). A similar observation is made for the impact melt particles M3 and M7 from Pop C6 (identified in Fig. 5A). All other impact melt particles analyzed in Pop C6 cluster together at slightly higher Fe_2O_3 and MgO concentrations relative to M3 and M7 (Fig. 10A). This difference between these two groups of impact melt particles can also be observed in the single-element heat maps (Fig. 3) and the photograph of Pop C6 (Fig. 1A). M3 and M7 are comparatively less porous and are characterized by entrained felsic basement clasts. Therefore, we interpret these clasts as microcrystalline impact melt particles that represent brecciated parts of clast-rich impact melt rock derived from melt bodies in the central part of the Popigai crater. The other melt clasts are interpreted as vitric impact melt particles. Their enrichment in Fe and Mg can be explained by the alteration of glass due to the formation of smectite, a common feature observed in many impact structures and also described in literature for Popigai (e.g., Masaitis et al.,

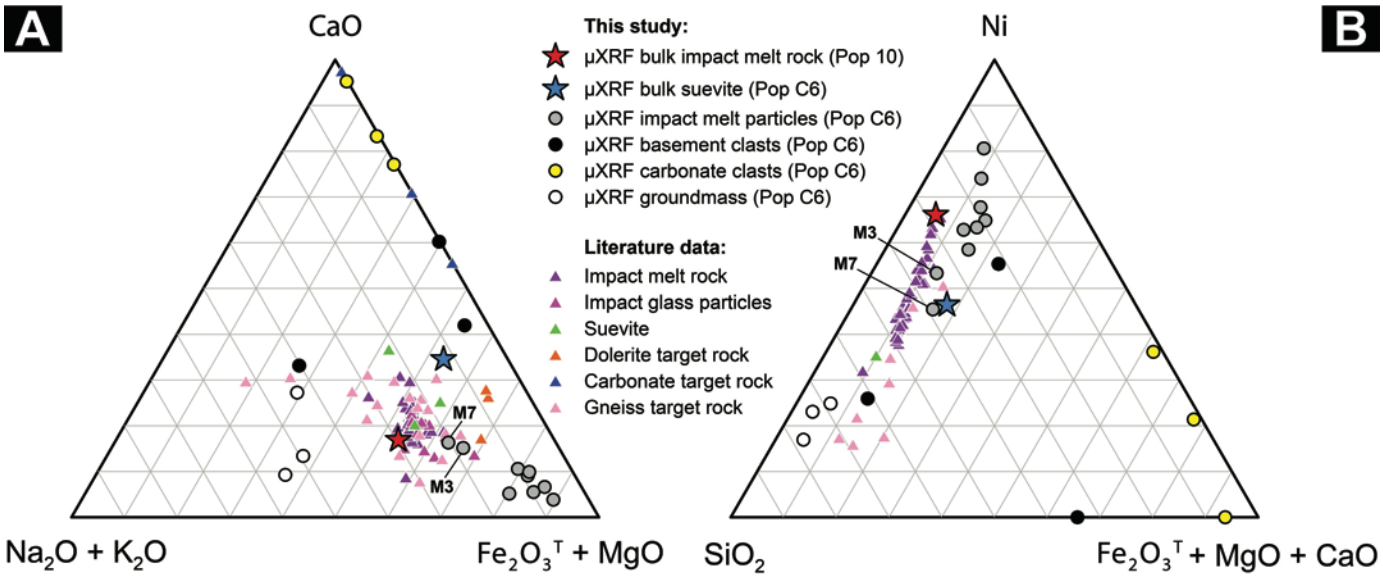

Figure 10. (A) Ternary $Na_2O + K_2O$–$Fe_2O_3^T$ + MgO–CaO diagram and (B) ternary SiO_2–$Fe_2O_3^T$ + MgO + CaO–Ni diagram showing bulk and clast-specific micro–X-ray fluorescence (μXRF) data from Pop 10 and Pop C6 (this work), compared to Popigai literature data of impact melt rock/particles, suevite, and target lithologies (from Rabkin, 1959; Lutz, 1985; Vishnevsky and Montanari, 1999; Whitehead et al., 2002; Kettrup et al., 2003; Tagle, 2004; Tagle and Claeys, 2005). Diagram in A is derived from Kettrup et al. (2003). $Fe_2O_3^T$ = total iron. Data are shown in Table A4.

2018). These vitric, altered greenish melt particles correspond to those found in the suevite described from the upper unit of the Popigai crater fill sequence (Naumov, 2002). The carbonate clast (C1, C2, and C3) compositions match well with the carbonate target rock (limestone) literature data (Fig. 10A; Kettrup et al., 2003). The groundmass area (G1, G2, and G3) concentrations fall within the range of the basement literature data but appear enriched in alkaline elements compared to the other clasts and bulk rock values (Fig. 10A). This could be due to the K-metasomatic hydrothermal overprint, which is known to affect large impact structures (e.g., Abramov and Kring, 2004) and has been observed at Popigai (Naumov, 2002). Figure 10B plots SiO_2 versus Fe_2O_3 + MgO + CaO and Ni, because Pop 10 and most of Pop C6 clasts display a Ni concentration above 50 ppm (even >100 ppm for most impact melt particles). The concentrations quantified by the μXRF SFP method for these oxides have been shown to be accurate (Figs. 8–9; Table 1), and for Ni, the concentrations are high enough to be meaningful (Fig. 8; Table 2). A good correspondence between the μXRF data and literature data is clear for the bulk Pop C6 and Pop 10, and for most of the impact melt particles of Pop C6, including the Ni values. The Ni concentrations of M3 and M7 are slightly lower than those of the other impact melt particles (Fig. 10B), which can be explained by larger felsic basement contributions to M3 and M7 (Fig. 3). The three groundmass areas analyzed are more enriched in SiO_2 than any other component within Pop C6 (Fig. 10B), which is also visible in the multi-element Fe-Si-Ca-K map and the Si heat map of the Popigai suevite sample (Fig. 3). This likely results from a significant incorporation and comminution of felsic lithologies in the groundmass, which are abundant within the different Popigai target rocks (Masaitis, 1994; Vishnevsky and Montanari, 1999).

Comparison among Chicxulub, Ries, and Popigai Samples

The Chicxulub samples were used to demonstrate that the μXRF SFP quantification provides accurate and precise data for most major elements (Figs. 8–9; Table 1). This is confirmed by the good agreement between the data obtained for the Popigai samples and the literature data for the major elements and also for Ni (Fig. 10; Table 2). Therefore, we compared the data obtained by μXRF SFP quantification on the bulk maps of the six samples shown in Figures 1 and 4A (Pop C6, Pop 10, Aum-01, Pols-01, 54_1_64_66, and 90_1_85_87). The ternary diagrams used for this purpose (Fig. 11) are identical to those shown in Figure 10. The compositions of lithologies from the three impact structures result from the mixing between a mafic, a felsic, and a sedimentary carbonate component (Fig. 11A), which is linked to a distinct target stratigraphy (e.g., Popigai—Masaitis, 1994; Vishnevsky and Montanari, 1999; Ries—Pohl et al., 1977; Schmidt-Kaler, 1978; Kring, 2005; Chicxulub—Kring, 2005; Keppie et al., 2011). The μXRF measurements of all the six crater impactites fall within or in close proximity to fields of bulk data from literature values of Chicxulub (Kettrup and Deutsch, 2003), Popigai (Kettrup et al., 2003), and Ries impactites (Siegert and Hecht, 2018), respectively. The small deviation for the suevite sample from Popigai (Pop C6) can be explained by the incorporation of carbonate clasts in this sample. Relative to each other, the Ries impactites are enriched in a felsic component, the Popigai impactites are enriched in a mafic component, and the

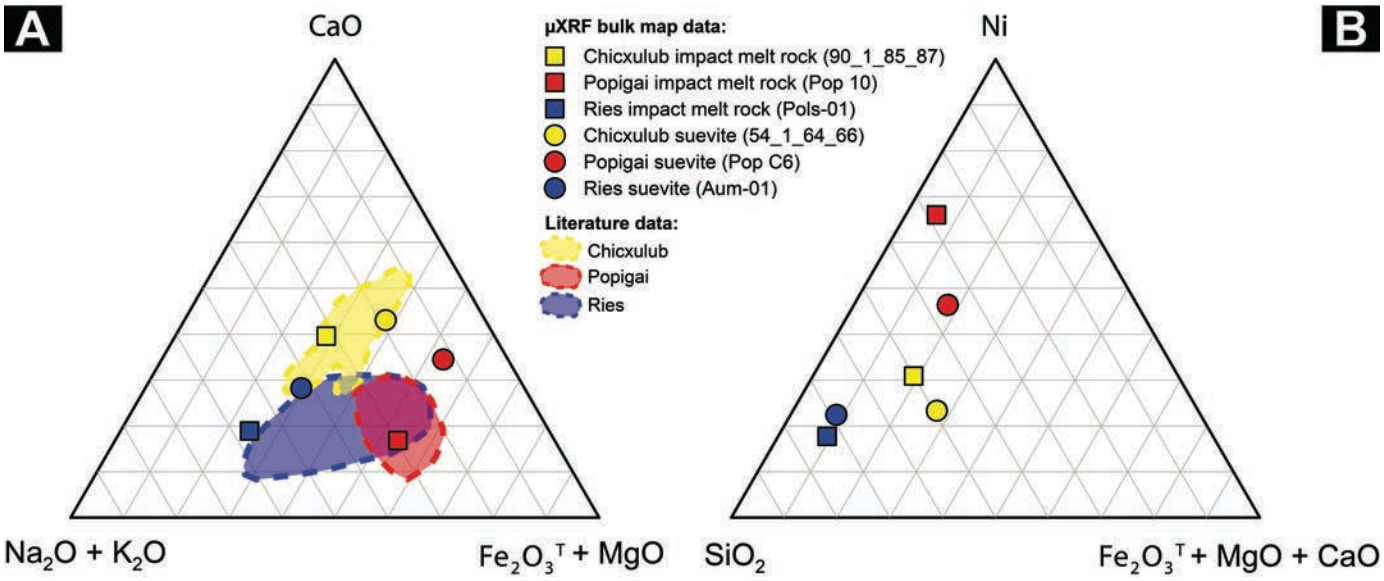

Figure 11. (A) Ternary $Na_2O + K_2O$–$Fe_2O_3^T$ + MgO–CaO diagram and (B) ternary SiO_2–$Fe_2O_3^T$ + MgO + CaO–Ni diagram showing bulk map micro–X-ray fluorescence (µXRF) data from representative impact melt rock and suevite samples from Chicxulub, Popigai, and Ries impact craters. Fields of literature major-element data are shown in A for impactites from Chicxulub (Kettrup and Deutsch, 2003), Popigai (Kettrup et al., 2003), and Ries (Siegert and Hecht, 2018). $Fe_2O_3^T$ = total iron. Data are shown in Table A4.

Chicxulub impactites are enriched in a carbonate component. For all three impact structures, the suevite samples are enriched in carbonate (as traced by elevated CaO concentrations) relative to the corresponding impact melt rocks (Fig. 11A). For these three impact structures, pre-impact sedimentary target rocks of different thicknesses (2.5–3 km for Chicxulub [Urrutia-Fucugauchi et al., 2011]; 1.5–1.7 km for Popigai [Vishnevsky and Montanari, 1999]; and 470–820 m for Ries [Schmidt-Kaler, 1978]) overlie crystalline basement lithologies. For all three craters, a carbonate component is part of the sedimentary cover, and for Chicxulub, the sedimentary target was composed of mostly carbonate and anhydrite. This explains the enrichment of the suevite samples in carbonate compared to the respective impact melt rocks, because the upper part of the impactite sequence incorporates more material from the upper part of the target stratigraphy. The main component of all these impactites is silicate melt, especially in the case of Ries (Fig. 11B). The Popigai impactites are more enriched in Ni than those at Chicxulub and Ries as described in the literature (Popigai—Tagle and Claeys, 2005; Chicxulub—Tagle et al., 2004; Ries—Siegert and Hecht, 2018). This observation can be explained by the presence of "up to several dozens of meters thick dolerite dykes and sills" (Kettrup et al., 2003, p. 735) within the Popigai target rocks, but it may also reflect a large meteoritic contribution (Tagle and Claeys, 2005). The two samples from Ries display similar Ni concentrations, which is in agreement with literature data (e.g., Siegert and Hecht, 2018). However, for Chicxulub and Popigai, the impact melt rocks are more enriched in Ni than the corresponding suevites. This is frequently observed for impact structures (e.g., Koeberl et al., 2007) and is generally interpreted to reflect a higher dilution of projectile components by (sedimentary) target rocks in the case of suevites (Goderis et al., 2012).

Benefits and Pitfalls of µXRF Compared to Other Quantitative Techniques

The µXRF SFP quantification method can accurately and precisely quantify major elements but tends to overestimate most of the trace-element concentrations in the case of thick samples. In the case of thin sections, the µXRF SFP quantification appears to be accurate and precise from Na to Ca, less reliable for Ti, Mn, and Fe, and not efficient in quantifying most trace elements. A comparison with other in situ semidestructive bulk techniques is presented in Table 3. For the purpose of this work, the limits of detection (LODs) for µXRF were estimated based on repeated measurements of the U.S. Geological Survey reference material basalt glass BCR-2G (Table 3). These estimates are conservative because the LODs strongly depend on the matrix and the homogeneity of the material studied (reference material or proximal impactites). Light elements (Na to P) have LODs ranging from ~7000 to 400 ppm, other major elements (K to Fe) show LODs ranging from ~70 to 20 ppm, and LODs for trace elements from Ni to Zr are all below 15 ppm (Table 3).

As a screening tool, µXRF outclasses scanning electron microscopy–energy-dispersive X-ray spectroscopy (SEM-EDS) for most of the characteristics, except the spatial resolution (Table 3). This study demonstrates that µXRF SFP quantification is a powerful technique, especially for the major elements. For a precise determination of trace-element concentrations, several in situ semidestructive techniques are recommended, such

TABLE 3. COMPARISON BETWEEN MICRO–X-RAY FLUORESCENCE (μXRF) AND FOUR OTHER IN SITU GEOCHEMICAL TECHNIQUES SUITABLE FOR MAJOR- AND TRACE-ELEMENT ANALYSIS OF GEOLOGICAL SAMPLES

	μXRF*	SEM-EDS§	EMPA (-WDS)§	LA-ICP-MS#	Synchrotron XRF**
Type of samples	Solid Liquid Powder	Solid	Solid	Solid	Solid
Spatial resolution	Micrometer to millimeter	50–100 nm	Micrometers	Micrometers	10–100 nm
Limit of detection	Na (6734), Mg (2164), Al (1021), Si (435), P (659), S (18), K (47), Ca (66), Ti (20), Cr (3), Mn (24), Fe (21), Ni (8), Cu (4), Zn (7), Ga (5), Rb (13), Sr (13), Y (9), Zr (15)††	From few hundreds of ppm	From few hundreds of ppm	From ppt to ppb	10–100 ppb
Range of elements	C–U	Na–U	Be–U	Li–U	Li–U
Sample size	Up to several hundreds of square centimeters (cm^2)	Standard-size 27 × 46 mm rectangular sections (often 30 μm thin sections) or 2.5 cm round epoxy disks	Standard-size 27 × 46 mm rectangular sections (often 30 μm thin sections) or 2.5 cm round epoxy disks	Depends on the size of the ablation cell	Up to several hundreds of square centimeters (cm^2)
Costs	Few euros/US dollars per day	Tens of euros/US dollars per day	Hundreds of euros/US dollars per day	Hundreds of euros/US dollars per day	Thousands of euros/US dollars per day
Sample preparation	Fast and limited	Samples must be: (1) flat and finely polished (2) coated (mostly by C)...	Samples must be: (1) flat and finely polished (2) coated (mostly by C). Samples in priority list with photomicrographs or maps of the regions of interest	Samples preferably flat and polished Samples in priority list with photomicrographs or maps of the regions of interest	Mounting in radiation chamber requires time, limited by stage, but allows all morphologies/surfaces
Measurement duration	~1 h to map 8 cm^2 and ~1 d for 320 cm^2 (1 ms for every 25 μm spot)	Less than 5 minutes/image for spot analysis	Depends on resolution but often several hours for thin sections	Mapping relatively fast in latest-generation cells	Depends on resolution but often several hours (time between shifts/recharge)
Limitations	Standardless and standardized method available	Qualitative and semiquantitative analysis	Must be standardized Possible to acquire 10–12 elements per analysis	Appropriate standardization for each session	Standardless and standardized method available

*Micro–X-ray fluorescence (μXRF) data from Beckhoff et al. (2006) and this study.
§Scanning electron microscopy–energy-dispersive X-ray spectroscopy (SEM-EDS) and electron probe microanalysis (EPMA) (with wavelength-dispersive spectrometry [WDS]) data from Reed (2005).
#Laser-ablation–inductively coupled plasma–mass spectrometry data from Van Malderen (2017).
**Synchrotron X-ray fluorescence (XRF) data from Laforce (2018).
††Limits of detection in ppm, calculated based on repeated measurements of the U.S. Geological Survey reference material basalt glass BCR-2G.

as LA-ICP-MS and synchrotron XRF (Table 3). However, the disadvantages of these techniques involve a smaller sample size, a longer sample preparation and measurement time, a necessity of standardization (not compulsory for synchrotron XRF), and a higher cost (Table 3). We therefore suggest to first perform μXRF mapping on geological samples as (1) a first geochemical characterization and (2) to be able to detect suitable areas for more in-depth research. Subsequently, these regions of interest on the sample surface can then be prepared for higher-resolution and more accurate measurements (including trace elements) by means of, for example, LA-ICP-MS.

The results presented in this study are based on the Bruker M4 μXRF instrument (installation in 2015 at the Vrije Universiteit Brussel; Fig. 1C), which uses intermediate-vacuum conditions (20 mbar) that make the mapping of lighter elements (from H to Na) difficult or impossible. However, later-generation μXRF instruments are now available that—due to better vacuum conditions—allow a more precise mapping of those elements (e.g., the Bruker M4 Tornado Plus with optional He-purge system to achieve <20 mbar vacuum conditions, which allow detection of C, N, O, F, and Na). Also, larger sample chambers exist, where, most of the time, the sample has a fixed position, and a single detector is moved across the sample surface (e.g., the Bruker M6 can acquire maps with an area of 80 cm × 60 cm at 100 μm resolution). Another difficulty associated with the XRF technique concerns the deconvolution of closely neighboring peaks. In the case of samples with, for example, high Fe contents and low Co peaks (or high Ti and low V concentrations), considerable data processing is required to obtain accurate Co results.

In general, the μXRF quantification can also be carried out by applying calibration curves, which require the incorporation of multiple homogeneous, matrix-matched reference materials. However, impactites are often heterogeneous in nature due to their complex emplacement mechanisms and the large variety of chemically distinct target lithologies incorporated in these samples. For example, the Pop C6 suevite consists of vitric impact melt particles intermediate to mafic in composition, granular to crystalline felsic basement clasts, and crystalline to mud-rich carbonate clasts. This wide range of clast matrices requires separate matrix-matched multiple-standard calibrations applied to the different groups of clasts. A multiple-standard calibration is not recommended for bulk quantification of impact breccia samples due to this large clast variability, and the μXRF SFP quantification can be considered to be sufficiently accurate and precise. The μXRF quantification of relatively homogeneous or simple impactites, such as clast-free to clast-poor impact melt rocks, could benefit from a fit-for-purpose matrix-matched calibration. Further research is needed in this field, as this endeavor would require the incorporation of a large set of international reference materials that can reflect the chemical variability encountered in target lithologies from preferably a large number of impact structures.

The μXRF technique presented in this study also has wider applications in other geoscience fields, such as the analysis of sedimentary or volcanic breccias, meteorites, and conglomerates. Such coarse-grained lithologies, often heterogeneous in nature, are particularly well suited for digital clast segmentation to quantify both bulk and clast-specific textural properties. In addition, the geochemical composition can be compared with these particle parameters such as clast size, shape, roundness, and degree of sorting. This implies that two extensive, independent data sets, derived from μXRF scanning and subsequent digital image analysis, can be obtained in a matter of hours.

CONCLUSIONS

In this study, we present an inexpensive, fast, high-resolution and nondestructive approach to geochemically characterize proximal impactites using μXRF. This technique allows rapid acquisition of the following data:

(1) Qualitative multi-element maps: These maps make μXRF an efficient screening tool because simple multi-element maps (e.g., Fe-Si-Ca) are often sufficient to disentangle various lithological components.

(2) Semiquantitative single-element heat maps: These maps allow the visualization of elemental distributions within the samples. Each heat map has a linear RGB-colored (0–255) scale, with the highest RGB value (255) determined by the pixel with the highest main fluorescence peak amplitude. When mapping multiple samples at the same time, this approach detects whether one sample is enriched in an element compared to another sample.

(3) Bulk geochemical data and clast-specific compositional data based on a manual selection of regions of interest: As such, μXRF is unique as a bulk technique that also allows characterization of geochemically specific areas. The quantification can rely on the standardless fundamental parameters method, which is accurate for most major elements (with Na_2O–CaO being accurate within 10% compared to bulk powder techniques) but tends to overestimate most trace-element concentrations for samples thicker than 1 mm. Regarding thin sections, the quantification is also accurate from Na to Ca, but less reliable in the cases of Ti, Mn, and Fe, and not useable to quantify trace elements due to their higher attenuation depth of the X-rays. Alternatively, matrix-specific calibration curves can be constructed using international reference materials.

(4) Quantitative image analysis, a semi-automatic tool of digital segmentation based on μXRF maps: Based on their geochemical composition, clasts can be segmented in an objective manner, unlike the use of visual characteristics (e.g., clast color). This technique results in an extensive quantitative data set of modal abundance, size, shape, and degree of sorting of the segmented clast population.

(5) Bulk and clast-specific geochemical data superimposed on clast-specific textural data: When thin

sections are mapped with this approach, the μXRF geochemical data set can also directly be integrated with mineralogical features. Such rapid, new workflows may also be adapted in geoscientific fields outside of impactite research to aid both in quantifying lithological components and in interpreting rock-forming processes.

In conclusion, we strongly recommend μXRF as both a visual screening tool and as a first quantitative geochemical tool for any new sample from known or potential impact structures.

ACKNOWLEDGMENTS

We appreciate the valuable comments of reviewers Martin Schmieder and Lutz Hecht, which helped to improve this manuscript. The Analytical, Environmental & Geo-Chemistry Research Unit team is supported by Research Foundation Flanders (FWO grant G0A6517), Belgian Science Policy Office (BELSPO BRAINS), the Excellence of Science Program (ET-HoME ID 30442502), and Vrije Universiteit Brussel (VUB) Strategic Research Program. Pim Kaskes thanks FWO for the awarded Ph.D. Fellowship (projects 11E6619N, 11E6621N). Philippe Claeys thanks the FWO-Hercules foundation for financing the X-ray fluorescence analytical platform at the VUB. We thank Niels J. de Winter for valuable discussions about the technical capabilities of the μXRF instrument.

APPENDIX

The material in the Appendix consists of μXRF major and trace element data sets that have been used in Figures 8 and 9 (Table A1–A3) and in Figures 10 and 11 (Table A4). In addition, Figure A1 and Table A5 show the attenuation depths of different minerals versus X-ray energies to provide additional explanation for the Discussion section "Differences between Thick and Thin Section Quantifications."

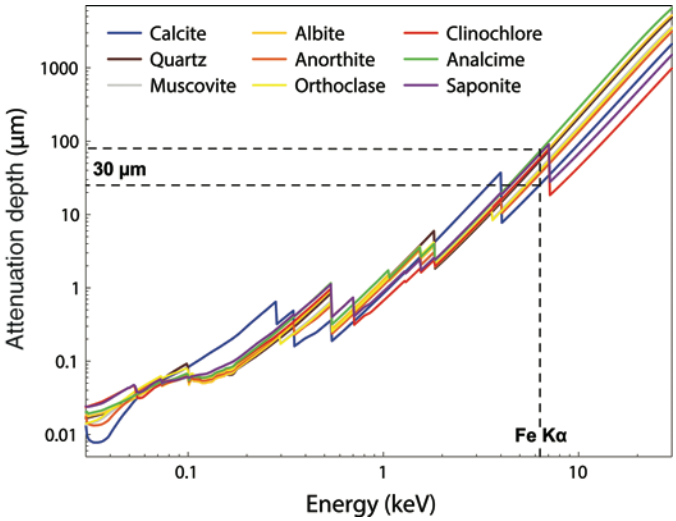

Figure A1. Nine mineral profiles of attenuation depth vs. X-ray energy. The intercepts are schematically indicated between the Fe Kα peak and range of attenuation depths for the different minerals. These intercepts lie around the maximum thickness of a geological thin section, i.e., 30 μm.

TABLE A1. RESULTS OF MICRO–X-RAY FLUORESCENCE (μXRF) STANDARDLESS FUNDAMENTAL PARAMETERS (SFP) QUANTIFICATION OF CHICXULUB IMPACTITE SAMPLES BASED ON SPOTANALYSIS ON POWDERS

Sample name	Lithology	Major elements as oxides (wt%)								
		Na_2O	MgO	Al_2O_3	SiO_2	K_2O	CaO	TiO_2	MnO	Fe_2O_3
40_2_0_3	Suevite	2.26	3.57	9.35	34.70	3.84	41.77	0.58	0.26	3.56
40_2_100_103	Suevite	2.37	5.51	9.23	36.35	2.90	37.38	0.56	0.24	5.32
44_1_46_48	Suevite	3.70	3.52	11.35	50.74	3.28	20.34	0.63	0.17	6.23
48_1_22_24	Suevite	2.84	4.46	11.51	50.01	3.83	19.15	0.66	0.13	7.38
51_1_12_14	Suevite	2.42	6.30	11.62	47.56	3.56	19.93	0.72	0.14	7.69
54_1_64_66	Suevite	3.00	6.33	11.69	49.86	2.68	16.65	0.81	0.14	8.78
56_1_95_97	Suevite	2.93	3.80	11.17	53.17	3.75	17.99	0.62	0.15	6.41
59_2_74_76	Suevite	2.37	5.61	11.28	46.22	3.49	23.03	0.66	0.23	7.05
67_1_13_15	Suevite	0.95	4.75	8.41	43.99	1.77	34.35	0.47	0.25	4.95
83_1_115_119	Suevite	1.21	4.86	5.64	23.70	0.77	57.79	0.44	0.22	5.15
84_3_117.5_119.5	UIMR	1.78	7.36	8.91	37.12	2.30	34.85	0.53	0.30	6.76
85_1_33_35	UIMR	2.22	9.41	14.80	47.29	1.56	6.00	1.55	0.24	16.92
86_1_9.5_11.5	UIMR	1.74	6.15	9.89	39.46	2.79	31.78	0.70	0.20	7.19
86_1_106_109	UIMR	4.16	3.27	16.46	60.28	3.97	4.69	0.80	0.09	6.28
87_2_38_41	UIMR	2.50	3.75	10.30	39.76	3.40	34.31	0.66	0.42	4.84
87_2_56_58	UIMR	3.18	3.55	12.28	43.03	3.06	28.28	0.80	0.26	5.50
87_2_103.5_107	UIMR	4.79	2.31	17.56	56.59	5.22	6.32	1.02	0.09	6.10
88_2_7_9	UIMR	4.33	1.65	16.59	63.00	5.24	4.09	0.77	0.04	4.29
89_1_57_59	UIMR	3.41	3.35	14.29	53.55	4.75	12.91	0.75	0.17	6.81
89_3_8_10	UIMR	4.05	1.71	15.69	58.51	5.83	7.44	0.77	0.14	5.86
90_1_85_87	UIMR	4.18	1.41	16.46	56.22	6.10	8.34	0.88	0.16	6.24
90_3_66_68	UIMR	2.85	5.66	13.16	50.29	4.31	13.09	0.80	0.18	9.63
91_2_87_89	UIMR	4.12	1.20	16.15	56.62	6.77	8.61	0.75	0.19	5.59
92_1_94_96	UIMR	3.86	2.26	15.48	56.68	5.96	8.14	0.77	0.19	6.65
93_1_19_21	UIMR	4.18	3.62	16.43	57.89	5.18	4.90	0.76	0.11	6.94
95_1_52_54	UIMR	4.13	2.36	17.53	56.74	5.46	6.64	0.79	0.08	6.26
95_2_89.5_91.5	Granitoid clast	4.41	0.39	12.05	76.07	4.07	1.03	0.23	0.02	1.74
95_3_55_57	UIMR	4.73	3.58	16.96	58.61	4.02	4.92	0.75	0.05	6.38
105_2_37_39	Felsite	2.95	4.50	15.31	54.21	6.45	7.84	1.04	0.16	7.29
140_2_19_21	Dolerite	B.D.L.	15.23	14.05	41.78	0.53	8.94	1.26	0.33	17.25
162_1_54_56	Dolerite	B.D.L.	16.32	13.11	40.85	0.68	6.44	1.73	0.49	19.71
238_2_0_2	Dacite	4.12	2.08	14.97	65.12	5.56	2.62	0.84	0.07	4.50
239_1_105_107	Felsite	2.97	6.04	14.86	53.81	4.54	7.92	0.83	0.13	8.60
276_3_93_95	Metamorphic clast	3.94	3.68	13.21	60.95	1.98	2.61	1.38	0.14	12.12
281_2_50_52	LIMR/suevite	4.39	4.03	14.92	62.90	3.48	2.11	0.69	0.12	7.35
282_1_80_82	LIMR/suevite	4.03	2.85	12.94	68.11	3.84	1.62	0.56	0.08	5.96
283_2_46_48	LIMR/suevite	4.03	6.43	14.22	59.99	2.78	2.16	0.67	0.13	9.60
288_1_75.5_77.5	Granitoid	5.74	0.68	13.03	73.66	3.00	1.64	0.58	0.03	1.63
295_3_2_4	Granitoid	4.85	B.D.L.	13.14	74.54	5.25	0.73	0.20	0.02	1.27
303_3_17.5_19.5	LIMR/suevite	4.14	5.00	15.13	60.00	3.54	2.10	0.85	0.11	9.12

Note: Table shows data that are used for the graphs in Figures 8 and 9A. Data are based on spotanalysis (using a 200 μm spotsize) of homogenized powders from 40 impactite drill core samples collected during the Chicxulub International Ocean Discovery Program–International Continental Drilling Project (IODP-ICDP) Expedition 364. UIMR—upper impact melt rock; LIMR—lower impact melt rock; B.D.L.—below detection limit.

Sample name	Lithology	Trace elements (ppm)								
		Cr	Ni	Cu	Zn	Ga	Rb	Sr	Y	Zr
40_2_0_3	Suevite	76	B.D.L.	41	107	B.D.L.	51	1853	13	82
40_2_100_103	Suevite	86	B.D.L.	47	73	8	25	1410	18	80
44_1_46_48	Suevite	60	29	65	88	13	41	993	20	137
48_1_22_24	Suevite	68	29	74	113	13	68	1057	21	176
51_1_12_14	Suevite	81	27	156	103	12	78	908	20	117
54_1_64_66	Suevite	96	31	86	108	22	51	1185	31	152
56_1_95_97	Suevite	60	27	49	100	13	62	905	23	136
59_2_74_76	Suevite	76	27	41	149	14	74	1114	29	136
67_1_13_15	Suevite	51	B.D.L.	25	100	6	28	2658	18	77
83_1_115_119	Suevite	55	B.D.L.	9	135	B.D.L.	B.D.L.	1850	16	65
84_3_117.5_119.5	UIMR	57	B.D.L.	B.D.L.	152	14	32	1185	18	154
85_1_33_35	UIMR	77	50	44	103	33	20	540	61	137
86_1_9.5_11.5	UIMR	93	37	B.D.L.	149	18	49	1583	21	155
86_1_106_109	UIMR	98	63	73	288	26	90	659	14	179
87_2_38_41	UIMR	70	B.D.L.	B.D.L.	132	12	84	857	24	146
87_2_56_58	UIMR	90	23	11	126	15	53	1137	18	166
87_2_103.5_107	UIMR	174	46	171	591	21	98	667	18	198
88_2_7_9	UIMR	83	54	59	279	26	124	621	14	167
89_1_57_59	UIMR	80	32	31	180	21	100	742	20	170
89_3_8_10	UIMR	80	29	40	116	22	128	525	22	176
90_1_85_87	UIMR	95	29	37	144	22	123	544	20	182
90_3_66_68	UIMR	97	37	123	139	27	88	833	27	173
91_2_87_89	UIMR	82	22	B.D.L.	122	25	133	468	19	205
92_1_94_96	UIMR	102	28	6	126	22	128	532	23	185
93_1_19_21	UIMR	64	34	44	138	25	112	573	23	194
95_1_52_54	UIMR	76	25	82	205	28	118	741	24	209
95_2_89.5_91.5	Granitoid clast	B.D.L.	28	12	93	30	136	765	B.D.L.	120
95_3_55_57	UIMR	68	34	32	137	36	83	793	19	213
105_2_37_39	Felsite	102	134	17	115	37	226	3101	48	312
140_2_19_21	Dolerite	623	299	152	161	39	B.D.L.	595	25	101
162_1_54_56	Dolerite	490	373	167	147	39	18	688	30	163
238_2_0_2	Dacite	7	23	76	104	52	290	1319	15	272
239_1_105_107	Felsite	83	124	B.D.L.	127	30	128	1910	50	321
276_3_93_95	Metamorphic clast	B.D.L.	B.D.L.	10	63	27	56	315	54	313
281_2_50_52	LIMR/suevite	39	28	33	90	31	126	406	16	192
282_1_80_82	LIMR/suevite	17	28	16	86	32	163	391	9	159
283_2_46_48	LIMR/suevite	38	32	81	145	38	99	519	18	158
288_1_75.5_77.5	Granitoid	20	25	11	43	42	116	500	18	206
295_3_2_4	Granitoid	4	27	B.D.L.	36	30	160	425	B.D.L.	93
303_3_17.5_19.5	LIMR/suevite	63	34	56	94	42	112	357	22	183

TABLE A2. RESULTS OF MICRO–X-RAY FLUORESCENCE (μXRF) STANDARDLESS FUNDAMENTAL PARAMETERS (SFP) QUANTIFICATION OF CHICXULUB IMPACTITE SAMPLES BASED ON MAPPING OF THICK SECTIONS

Sample name	Lithology	Major elements as oxides (wt%)								
		Na_2O	MgO	Al_2O_3	SiO_2	K_2O	CaO	TiO_2	MnO	Fe_2O_3
40_2_0_3	Suevite	2.91	2.24	10.35	35.87	3.93	39.27	0.91	0.27	4.23
40_2_100_103	Suevite	3.34	3.41	9.63	37.70	3.20	36.22	0.74	0.25	5.45
44_1_46_48	Suevite	4.19	3.02	11.35	50.96	2.89	18.61	0.81	0.17	8.00
48_1_22_24	Suevite	5.02	4.20	11.93	50.29	3.20	14.99	0.83	0.13	9.41
51_1_12_14	Suevite	4.11	4.09	13.08	51.86	3.43	14.00	0.86	0.13	8.43
54_1_64_66	Suevite	3.91	4.10	12.21	51.69	2.69	15.14	0.85	0.15	9.27
56_1_95_97	Suevite	3.71	4.32	11.88	47.99	3.01	18.81	0.88	0.19	9.22
59_2_74_76	Suevite	3.91	3.72	13.14	48.59	3.13	19.14	0.74	0.15	7.49
67_1_13_15	Suevite	2.79	6.15	13.02	51.93	2.12	14.19	1.13	0.12	8.56
83_1_115_119	Suevite	2.96	3.93	5.90	23.55	0.36	57.72	0.59	0.20	4.68
84_3_117.5_119.5	UIMR	4.91	5.64	10.68	40.82	1.82	28.75	0.76	0.15	6.45
85_1_33_35	UIMR	3.64	7.35	15.62	50.85	1.30	6.04	1.03	0.18	13.98
86_1_9.5_11.5	UIMR	4.25	4.43	14.88	53.25	2.78	12.76	0.92	0.09	6.64
86_1_106_109	UIMR	4.91	2.16	15.61	65.07	2.71	4.35	0.69	0.07	4.43
87_2_38_41	UIMR	4.03	2.55	13.14	47.34	3.11	24.17	0.80	0.12	4.74
87_2_56_58	UIMR	4.30	3.88	15.18	50.19	2.54	14.26	1.13	0.11	8.38
87_2_103.5_107	UIMR	4.41	1.09	17.26	59.26	6.09	7.09	0.93	0.07	3.80
88_2_7_9	UIMR	4.74	0.39	11.79	74.01	5.30	2.08	0.31	0.03	1.36
89_1_57_59	UIMR	3.78	3.37	14.09	52.03	3.82	14.98	0.85	0.16	6.93
89_3_8_10	UIMR	4.51	1.68	14.99	61.85	4.71	6.49	0.69	0.11	4.95
90_1_85_87	UIMR	4.19	1.84	16.18	52.95	5.21	11.73	1.06	0.21	6.63
90_3_66_68	UIMR	4.67	2.91	16.23	55.49	4.52	6.97	1.01	0.16	8.04
91_2_87_89	UIMR	4.53	1.58	16.57	56.16	5.69	8.58	0.85	0.18	5.87
92_1_94_96	UIMR	3.85	1.98	14.22	49.50	4.49	18.24	0.87	0.33	6.52
93_1_19_21	UIMR	4.89	2.77	16.69	58.60	4.65	4.58	0.82	0.12	6.88
95_1_52_54	UIMR	5.44	3.04	17.60	56.12	3.56	5.91	0.95	0.08	7.29
95_2_89.5_91.5	Granitoid clast	5.41	0.59	12.90	74.64	3.76	1.29	0.18	0.02	1.22
95_3_55_57	UIMR	5.19	2.74	17.69	59.25	3.62	4.02	0.84	0.05	6.62
105_2_37_39	Felsite	3.48	4.08	14.77	57.17	5.28	6.62	1.13	0.15	7.17
140_2_19_21	Dolerite	1.62	11.83	15.93	44.14	0.48	7.66	1.18	0.32	16.83
162_1_54_56	Dolerite	1.53	14.03	14.24	40.78	0.61	5.59	1.68	0.42	21.10
238_2_0_2	Dacite	5.84	1.07	16.49	65.74	4.95	2.43	0.55	0.06	2.87
239_1_105_107	Felsite	3.58	4.31	15.17	56.03	4.25	7.28	0.92	0.14	8.23
276_3_93_95	Metamorphic clast	4.50	3.52	13.01	61.26	1.02	2.72	1.27	0.17	12.52
281_2_50_52	LIMR /suevite	4.82	3.33	14.68	64.76	3.03	2.03	0.61	0.13	6.61
282_1_80_82	LIMR /suevite	4.95	3.54	14.35	63.96	3.35	1.92	0.67	0.13	7.15
283_2_46_48	LIMR /suevite	7.37	5.18	14.52	58.18	2.25	2.16	0.73	0.13	9.47
288_1_75.5_77.5	Granitoid	8.23	B.D.L.	15.52	68.96	5.34	1.07	0.16	0.02	0.70
295_3_2_4	Granitoid	4.38	0.52	12.25	75.53	4.87	0.79	0.32	0.03	1.31
303_3_17.5_19.5	LIMR /suevite	4.39	4.23	15.75	59.86	3.01	2.24	0.87	0.12	9.54

Note: Table shows data that are used for the graphs in Figures 8 and 9B. Data are based on mapping of thick sections from 40 impactite drill core samples collected during the Chicxulub International Ocean Discovery Program–International Continental Drilling Project (IODP-ICDP) Expedition 364. UIMR—upper impact melt rock; LIMR—lower impact melt rock; B.D.L.—below detection limit.

Sample name	Lithology	Trace elements (ppm)								
		Cr	Ni	Cu	Zn	Ga	Rb	Sr	Y	Zr
40_2_0_3	Suevite	118	26	48	74	35	107	2661	22	167
40_2_100_103	Suevite	89	19	71	65	38	77	2148	28	167
44_1_46_48	Suevite	103	16	55	95	29	69	1269	32	193
48_1_22_24	Suevite	129	25	66	113	27	106	1396	31	190
51_1_12_14	Suevite	118	38	66	109	26	109	1299	41	203
54_1_64_66	Suevite	117	24	78	112	36	95	1503	43	231
56_1_95_97	Suevite	121	26	38	124	27	108	1300	39	202
59_2_74_76	Suevite	91	19	21	99	35	112	1692	25	180
67_1_13_15	Suevite	142	40	73	121	37	99	4888	36	228
83_1_115_119	Suevite	22	28	9	87	39	B.D.L.	1531	17	84
84_3_117.5_119.5	UIMR	36	19	B.D.L.	116	33	47	1142	22	138
85_1_33_35	UIMR	102	57	85	104	28	35	468	34	97
86_1_9.5_11.5	UIMR	81	25	B.D.L.	111	37	53	1113	24	175
86_1_106_109	UIMR	27	22	67	193	21	50	522	18	118
87_2_38_41	UIMR	47	23	B.D.L.	100	34	101	811	19	176
87_2_56_58	UIMR	113	22	15	136	43	97	1286	41	292
87_2_103.5_107	UIMR	78	12	5	139	28	119	637	19	175
88_2_7_9	UIMR	4	24	B.D.L.	44	17	146	453	B.D.L.	157
89_1_57_59	UIMR	105	24	19	198	29	151	961	33	229
89_3_8_10	UIMR	37	18	53	93	21	104	386	23	160
90_1_85_87	UIMR	141	32	14	182	28	173	674	31	253
90_3_66_68	UIMR	126	36	88	122	30	133	787	38	237
91_2_87_89	UIMR	97	26	B.D.L.	123	28	166	679	30	231
92_1_94_96	UIMR	76	28	6	126	27	160	610	36	219
93_1_19_21	UIMR	92	30	69	137	30	142	651	35	228
95_1_52_54	UIMR	104	34	61	204	38	116	961	39	254
95_2_89.5_91.5	Granitoid clast	B.D.L.	10	B.D.L.	28	19	122	800	B.D.L.	60
95_3_55_57	UIMR	104	29	51	146	41	121	884	30	246
105_2_37_39	Felsite	121	121	B.D.L.	121	30	269	3237	58	382
140_2_19_21	Dolerite	735	418	156	125	43	36	763	33	121
162_1_54_56	Dolerite	713	484	179	150	51	32	788	46	192
238_2_0_2	Dacite	B.D.L.	14	35	72	36	276	1538	B.D.L.	190
239_1_105_107	Felsite	104	108	B.D.L.	121	35	190	2535	67	411
276_3_93_95	Metamorphic clast	B.D.L.	10	23	90	31	47	450	73	389
281_2_50_52	LIMR/suevite	28	20	B.D.L.	85	30	149	447	16	180
282_1_80_82	LIMR/suevite	35	30	11	93	32	171	687	21	197
283_2_46_48	LIMR/suevite	53	24	114	139	37	120	641	22	203
288_1_75.5_77.5	Granitoid	B.D.L.	12	B.D.L.	24	27	209	785	B.D.L.	93
295_3_2_4	Granitoid	B.D.L.	20	B.D.L.	39	20	179	506	B.D.L.	98
303_3_17.5_19.5	LIMR/suevite	50	35	56	104	51	130	443	33	225

TABLE A3. RESULTS OF MICRO–X-RAY FLUORESCENCE (μXRF) STANDARDLESS FUNDAMENTAL PARAMETERS (SFP) QUANTIFICATION OF CHICXULUB IMPACTITE SAMPLES BASED ON MAPPING OF THIN SECTIONS

Sample name	Lithology	Major elements as oxides (wt%)								
		Na_2O	MgO	Al_2O_3	SiO_2	K_2O	CaO	TiO_2	MnO	Fe_2O_3
40_2_0_3	Suevite	2.89	2.51	10.75	37.90	3.82	39.73	0.61	0.21	1.58
40_2_100_103	Suevite	2.89	3.62	10.67	43.24	3.15	33.07	0.60	0.18	2.56
44_1_46_48	Suevite	4.23	3.11	12.35	56.52	3.15	16.93	0.67	0.10	2.95
48_1_22_24	Suevite	3.13	5.27	12.99	57.07	3.29	14.74	0.60	0.06	2.85
51_1_12_14	Suevite	3.45	4.34	13.59	56.50	3.66	15.36	0.59	0.08	2.42
54_1_64_66	Suevite	3.82	4.85	13.68	57.57	2.88	12.71	0.72	0.08	3.69
56_1_95_97	Suevite	3.85	4.42	13.50	57.94	3.30	13.69	0.60	0.07	2.63
59_2_74_76	Suevite	3.43	4.80	13.21	52.38	3.11	19.14	0.60	0.10	3.25
67_1_13_15	Suevite	1.57	6.09	9.13	48.54	1.37	28.44	0.52	0.24	4.09
83_1_115_119	Suevite	2.32	4.50	5.92	27.53	0.54	55.74	0.54	0.21	2.63
84_3_117.5_119.5	UIMR	3.30	5.91	11.68	51.17	2.25	22.22	0.62	0.08	2.77
85_1_33_35	UIMR	4.25	7.19	16.48	56.79	1.40	7.83	0.87	0.09	5.10
86_1_9.5_11.5	UIMR	3.88	4.87	14.35	57.05	2.66	13.10	0.71	0.05	3.33
86_1_106_109	UIMR	5.63	1.69	14.83	68.35	2.07	4.63	0.52	0.05	2.24
87_2_38_41	UIMR	3.65	2.68	12.45	47.86	2.97	27.80	0.61	0.10	1.89
87_2_56_58	UIMR	4.50	3.27	15.64	52.96	2.66	15.52	0.92	0.09	4.45
87_2_103.5_107	UIMR	5.10	0.53	17.37	62.05	5.99	6.67	0.67	0.04	1.59
88_2_7_9	UIMR	4.38	0.39	14.88	70.56	5.59	2.56	0.40	0.02	1.22
89_1_57_59	UIMR	4.05	4.31	14.46	52.69	3.45	15.92	0.72	0.12	4.28
89_3_8_10	UIMR	5.03	1.35	14.73	65.99	4.22	6.83	0.40	0.04	1.42
90_1_85_87	UIMR	4.68	1.57	16.88	54.95	5.27	11.57	0.94	0.16	3.97
90_3_66_68	UIMR	4.71	2.77	16.51	58.54	4.73	7.13	0.84	0.12	4.65
91_2_87_89	UIMR	4.67	1.68	16.79	56.97	5.85	9.13	0.81	0.15	3.94
92_1_94_96	UIMR	4.31	2.24	15.73	56.82	4.98	10.72	0.75	0.18	4.28
93_1_19_21	UIMR	4.72	3.18	17.38	60.34	4.79	5.09	0.72	0.08	3.70
95_1_52_54	UIMR	5.15	3.28	18.57	59.03	3.58	6.28	0.72	0.05	3.34
95_2_89.5_91.5	Granitoid clast	4.76	0.46	10.55	78.41	3.08	1.87	0.22	0.02	0.64
95_3_55_57	UIMR	5.01	2.92	17.15	62.18	3.65	4.24	0.74	0.04	4.06
105_2_37_39	Felsite	4.28	2.74	14.69	60.98	5.48	8.25	0.76	0.07	2.59
140_2_19_21	Dolerite	2.48	11.16	18.22	47.87	0.58	8.96	1.16	0.22	9.34
162_1_54_56	Dolerite	2.31	12.62	16.13	53.08	0.91	9.70	0.95	0.13	4.16
238_2_0_2	Dacite	6.24	0.44	14.81	69.36	4.80	2.59	0.38	0.03	1.34
239_1_105_107	Felsite	4.21	3.31	14.12	59.56	4.51	8.71	0.68	0.09	4.58
276_3_93_95	Metamorphic clast	4.96	3.16	12.29	68.48	1.18	3.29	0.96	0.09	5.58
281_2_50_52	LIMR/suevite	5.72	3.48	14.40	67.12	2.73	4.11	0.40	0.05	1.99
282_1_80_82	LIMR/suevite	4.66	3.42	14.11	68.99	3.24	3.32	0.35	0.04	1.86
283_2_46_48	LIMR/suevite	5.31	4.63	13.96	66.57	2.38	3.89	0.44	0.05	2.77
288_1_75.5_77.5	Granitoid	6.65	B.D.L.	14.55	70.83	5.66	1.75	0.12	0.01	0.43
295_3_2_4	Granitoid	5.43	B.D.L.	14.15	72.45	5.56	1.67	0.17	0.01	0.47
303_3_17.5_19.5	LIMR/suevite	4.91	3.58	15.21	65.78	3.14	3.19	0.59	0.06	3.53

Note: Table shows data that are used for the graphs in Figures 8 and 9C. Data are based on mapping of thin sections from 40 impactite drill core samples collected during the Chicxulub International Ocean Discovery Program–International Continental Drilling Project (IODP–ICDP) Expedition 364. UIMR—upper impact melt rock; LIMR—lower impact melt rock; B.D.L.—below detection limit.

Sample name	Lithology	Trace elements (ppm)								
		Cr	Ni	Cu	Zn	Ga	Rb	Sr	Y	Zr
40_2_0_3	Suevite	62	15	20	42	29	38	447	B.D.L.	234
40_2_100_103	Suevite	62	13	18	41	30	31	361	B.D.L.	222
44_1_46_48	Suevite	47	B.D.L.	18	41	24	30	218	B.D.L.	230
48_1_22_24	Suevite	52	B.D.L.	23	35	24	29	198	B.D.L.	170
51_1_12_14	Suevite	60	B.D.L.	12	33	20	25	195	B.D.L.	162
54_1_64_66	Suevite	72	9	21	38	26	28	209	B.D.L.	182
56_1_95_97	Suevite	45	9	17	38	25	26	190	B.D.L.	200
59_2_74_76	Suevite	50	10	19	42	23	30	233	B.D.L.	193
67_1_13_15	Suevite	37	25	13	60	22	49	760	B.D.L.	163
83_1_115_119	Suevite	B.D.L.	26	11	58	36	48	361	B.D.L.	206
84_3_117.5_119.5	UIMR	25	9	6	41	25	30	209	B.D.L.	101
85_1_33_35	UIMR	55	19	6	32	21	22	129	B.D.L.	81
86_1_9.5_11.5	UIMR	57	10	B.D.L.	42	24	21	211	B.D.L.	97
86_1_106_109	UIMR	5	11	6	50	14	18	109	B.D.L.	60
87_2_38_41	UIMR	7	13	B.D.L.	39	25	35	192	B.D.L.	109
87_2_56_58	UIMR	66	15	B.D.L.	46	22	43	265	B.D.L.	205
87_2_103.5_107	UIMR	38	B.D.L.	B.D.L.	42	17	22	124	B.D.L.	82
88_2_7_9	UIMR	23	17	B.D.L.	23	14	42	156	B.D.L.	144
89_1_57_59	UIMR	85	17	19	64	20	45	269	B.D.L.	224
89_3_8_10	UIMR	16	B.D.L.	B.D.L.	24	15	24	98	B.D.L.	67
90_1_85_87	UIMR	110	20	15	74	17	49	218	B.D.L.	144
90_3_66_68	UIMR	96	20	66	55	17	41	215	B.D.L.	188
91_2_87_89	UIMR	90	21	21	57	18	50	202	B.D.L.	176
92_1_94_96	UIMR	80	16	B.D.L.	52	17	50	208	B.D.L.	178
93_1_19_21	UIMR	74	17	19	50	17	40	183	B.D.L.	158
95_1_52_54	UIMR	58	16	15	61	19	33	193	B.D.L.	187
95_2_89.5_91.5	Granitoid clast	B.D.L.	12	B.D.L.	26	12	22	104	B.D.L.	58
95_3_55_57	UIMR	80	23	22	66	22	36	220	B.D.L.	155
105_2_37_39	Felsite	49	36	B.D.L.	32	18	34	257	B.D.L.	131
140_2_19_21	Dolerite	466	117	46	52	19	33	241	B.D.L.	147
162_1_54_56	Dolerite	168	50	11	27	21	25	143	B.D.L.	144
238_2_0_2	Dacite	B.D.L.	B.D.L.	14	27	15	37	169	B.D.L.	98
239_1_105_107	Felsite	57	53	B.D.L.	51	21	41	328	B.D.L.	150
276_3_93_95	Metamorphic clast	B.D.L.	B.D.L.	B.D.L.	33	14	25	123	B.D.L.	99
281_2_50_52	LIMR/suevite	B.D.L.	B.D.L.	B.D.L.	23	14	24	104	B.D.L.	77
282_1_80_82	LIMR/suevite	5	B.D.L.	B.D.L.	22	14	22	109	B.D.L.	73
283_2_46_48	LIMR/suevite	11	B.D.L.	5	29	15	23	104	B.D.L.	101
288_1_75.5_77.5	Granitoid	B.D.L.	B.D.L.	B.D.L.	17	15	27	111	B.D.L.	62
295_3_2_4	Granitoid	B.D.L.	B.D.L.	B.D.L.	14	11	27	100	B.D.L.	92
303_3_17.5_19.5	LIMR/suevite	19	B.D.L.	11	28	17	20	103	B.D.L.	111

TABLE A4. RESULTS OF MICRO–X-RAY FLUORESCENCE (μXRF) STANDARDLESS FUNDAMENTAL PARAMETERS (SFP) QUANTIFICATION ON POPIGAI, CHICXULUB, AND RIES SAMPLES

Sample name	Major elements as oxides (wt%)						Trace elements (ppm)
	Na_2O	MgO	SiO_2	K_2O	CaO	Fe_2O_3	Ni
Popigai							
Pop 10 (bulk)	2.36	2.37	64.65	3.29	3.22	7.85	151
Pop C6 (bulk)	1.24	6.61	54.51	2.52	10.64	9.80	70
Pop C6-M3	3.99	5.36	55.79	0.47	3.72	11.03	86
Pop C6-M4	0.37	9.19	40.82	2.15	2.39	21.95	136
Pop C6-M5	1.58	6.94	48.68	2.69	1.53	16.89	124
Pop C6-M6	B.D.L.	7.42	46.79	2.83	2.88	18.51	106
Pop C6-M7	3.43	4.76	52.35	1.94	4.30	11.90	61
Pop C6-M8	0.16	7.01	43.25	3.19	3.52	19.40	125
Pop C6-M9	B.D.L.	7.80	44.93	2.65	3.18	18.46	307
Pop C6-M10	0.87	11.12	44.96	1.46	1.33	19.85	161
Pop C6-M11	B.D.L.	8.40	43.38	3.14	1.79	19.22	206
Pop C6-B2	6.66	1.75	56.19	1.39	6.63	3.57	24
Pop C6-B3	0.00	6.49	30.98	0.12	35.84	17.08	B.D.L.
Pop C6-B4	1.62	5.78	36.62	0.23	17.22	16.20	93
Pop C6-C1	0.29	14.68	1.90	0.16	79.75	0.88	26
Pop C6-C2	0.13	20.90	2.75	0.19	73.34	0.57	55
Pop C6-C3	B.D.L.	2.20	5.83	0.18	83.29	1.77	B.D.L.
Pop C6-G1	0.68	1.37	75.89	4.85	3.46	2.33	27
Pop C6-G2	1.49	1.72	79.24	3.78	1.43	2.25	17
Pop C6-G3	1.21	1.47	80.38	4.10	0.90	2.00	25
Chicxulub							
54_1_64_66 (bulk)	3.90	4.10	51.63	2.68	15.12	9.25	24
90_1_85_87 (bulk)	4.19	1.83	52.86	5.20	11.71	6.61	32
Ries							
Aum-01 (bulk)	2.80	0.51	66.35	3.29	4.09	3.76	22
Pols-01 (bulk)	3.28	0.22	60.77	6.82	3.38	4.13	15

Note: Table shows data from the μXRF SFP quantification of bulk maps and regions of interest of Popigai (Pop 10 and Pop C6), Chicxulub (54_1_64_66 and 90_1_85_87), and Ries (Aum-01 and Pols-01) samples. Clasts of Pop C6 are identified in Figure 5A. Data were used for the ternary diagrams in Figures 10 and 11. B.D.L.—below detection limit.

TABLE A5. INTERCEPTS OF THE ATTENUATION DEPTHS PER Kα PEAK (FROM Na to Zr)

Element	Kα1	Intercept* (μm)								
	(keV)	Calcite	Quartz	Muscovite	Albite	Anorthite	Orthoclase	Analcime	Saponite	Clinochlore
Na	1.040	0.926	1.308	1.220	1.435	1.200	1.296	1.649	0.983	0.733
Mg	1.254	1.513	2.159	2.006	1.871	1.971	2.127	2.071	1.577	1.168
Al	1.486	2.372	3.414	3.168	2.945	3.103	3.356	3.258	2.211	1.671
Si	1.740	3.655	5.281	2.670	3.323	2.733	3.737	3.544	2.298	2.148
P	2.010	5.451	2.291	2.462	2.404	2.573	2.646	2.967	3.039	2.448
S	2.309	8.020	3.264	3.529	3.440	3.692	3.785	4.256	4.380	3.520
Cl	2.622	11.443	4.563	4.955	4.824	5.184	5.305	5.979	6.167	4.946
Ar	2.958	16.044	6.314	6.878	6.691	7.193	7.353	8.305	8.571	6.859
K	3.314	22.071	8.621	9.410	9.155	9.838	10.047	11.376	11.730	9.369
Ca	3.692	29.890	11.642	9.150	12.383	13.295	8.778	15.403	15.850	12.634
Sc	4.093	7.963	15.562	12.201	16.576	10.771	11.687	20.638	19.540	16.843
Ti	4.512	10.261	20.527	16.042	21.891	14.044	15.341	27.280	25.678	22.136
V	4.953	13.131	26.810	20.871	28.622	18.155	19.924	**35.694**	**33.397**	28.782
Cr	5.415	16.674	**34.659**	26.865	**37.037**	23.257	25.601	46.221	42.981	**37.020**
Mn	5.900	21.037	44.436	**34.292**	47.525	29.571	**32.625**	59.349	54.837	47.193
Fe	6.405	26.331	56.429	43.345	60.401	**37.271**	41.169	75.472	69.282	59.563
Co	6.931	**32.720**	71.057	54.315	76.115	46.608	51.504	95.159	86.775	74.511
Ni	7.480	40.420	88.861	67.591	95.251	57.909	63.990	119.144	31.441	20.739
Cu	8.046	49.527	110.116	83.650	118.109	71.332	79.138	147.805	37.966	24.987
Zn	8.637	60.394	135.704	102.962	145.644	87.413	97.347	182.342	45.734	30.043
Ga	9.251	73.255	166.241	125.815	178.517	106.515	118.844	223.589	54.908	36.011
Ge	9.886	88.346	202.354	151.764	217.411	129.009	143.008	272.401	65.654	42.999
As	10.543	105.990	244.887	182.775	263.238	155.396	171.992	329.925	78.204	51.156
Se	11.224	126.591	294.878	219.532	317.120	186.300	206.412	397.567	92.841	60.667
Br	11.924	150.379	352.940	262.148	379.721	222.081	246.302	476.157	109.728	71.636
Kr	12.648	177.916	420.498	311.661	452.577	263.604	292.632	567.612	129.264	84.322
Rb	13.396	209.662	498.710	368.917	536.934	311.576	346.196	673.485	151.773	98.937
Sr	14.165	245.996	588.512	434.607	633.801	366.574	407.648	795.016	177.523	115.654
Y	14.958	287.592	691.548	509.947	744.938	429.624	478.137	934.385	206.991	134.783
Zr	15.775	335.069	809.334	596.066	871.984	501.673	558.727	1093.616	240.611	156.605

Note: Bold font indicates when the attenuation depth exceeds the thickness of a geological thin section (30 μm). Attenuation depth profiles are shown in Figure A1.

*Intercept calculated with method described by Henke et al. (1993).

REFERENCES CITED

Abramov, O., and Kring, D.A., 2004, Numerical modeling of an impact-induced hydrothermal system at the Sudbury crater: Journal of Geophysical Research, v. 109, no. E10, E10007, https://doi.org/10.1029/2003JE002213.

Alvarez, L.W., Alvarez, W., Asaro, F., and Michel, H.V., 1980, Extraterrestrial cause for the Cretaceous-Tertiary extinction: Science, v. 208, no. 4448, p. 1095–1108, https://doi.org/10.1126/science.208.4448.1095.

Artemieva, N.A., Wünnemann, K., Krien, F., Reimold, W.U., and Stöffler, D., 2013, Ries crater and suevite revisited—Observations and modeling, Part II: Modeling: Meteoritics & Planetary Science, v. 48, no. 4, p. 590–627, https://doi.org/10.1111/maps.12085.

Beckhoff, B., Kanngießer, B., Langhoff, N., Wedell, R., and Wolff, H., eds., 2006, Handbook of Practical X-Ray Fluorescence Analysis: Berlin, Springer, 863 p., https://doi.org/10.1007/978-3-540-36722-2.

Chanou, A., Osinski, G.R., and Grieve, R.A.F., 2014, A methodology for the semi-automatic digital image analysis of fragmental impactites: Meteoritics & Planetary Science, v. 49, no. 4, p. 621–635, https://doi.org/10.1111/maps.12267.

de Graaff, S.J., Kaskes, P., Déhais, T., Goderis, S., Debaille, V., Feignon, J.-G., Ferrière, L., Koeberl, C., Ross, C.H., and Claeys, Ph., 2019, Making (more) sense of destruction—A comprehensive geochemical investigation of Chicxulub impactites recovered during IODP-ICDP Expedition 364, *in* Reimold, W.U., convener, Large Meteorite Impacts and Planetary Evolution VI: Lunar and Planetary Institute Contribution 2136, abstract 5079.

de Winter, N.J., and Claeys, Ph., 2017, Micro X-ray fluorescence (μXRF) line scanning on Cretaceous rudist bivalves: A new method for reproducible trace element profiles in bivalve calcite: Sedimentology, v. 64, no. 1, p. 231–251, https://doi.org/10.1111/sed.12299.

de Winter, N.J., Sinnesael, M., Makarona, C., Vansteenberge, S., and Claeys, Ph., 2017, Trace element analyses of carbonates using portable and micro-X-ray fluorescence: Performance and optimization of measurement parameters and strategies: Journal of Analytical Atomic Spectrometry, v. 32, p. 1211–1223, https://doi.org/10.1039/C6JA00361C.

Déhais, T., Kaskes, P., de Graaff, S.J., Chernonozhkin, S.M., Debaille, V., Vanhaecke, F., Claeys, Ph., and Goderis, S., 2019, Disentangling cratering processes using non-traditional isotope ratios on core M0077A of the IODP-ICDP Expedition 364 in the Chicxulub impact structure, *in* Reimold, W.U., convener, Large Meteorite Impacts and Planetary Evolution VI: Lunar and Planetary Institute Contribution 2136, abstract 5106.

Dressler, B.O., and Reimold, W.U., 2001, Terrestrial impact melt rocks and glasses: Earth-Science Reviews, v. 56, no. 1–4, p. 205–284, https://doi.org/10.1016/S0012-8252(01)00064-2.

Floran, R.J., Grieve, R.A.F., Phinney, W.C., Warner, J.L., Simonds, C.H., Blanchard, D.P., and Dence, M.R., 1978, Manicouagan impact melt, Quebec: 1. Stratigraphy, petrology, and chemistry: Journal of Geophysical Research–Solid Earth, v. 83, no. B6, p. 2737–2759, https://doi.org/10.1029/JB083iB06p02737.

Flude, S., Haschke, M., and Storey, M., 2017, Application of benchtop micro-XRF to geological materials: Mineralogical Magazine, v. 81, no. 4, p. 923–948, https://doi.org/10.1180/minmag.2016.080.150.

French, B.M., 1998, Traces of Catastrophe: A Handbook of Shock-Metamorphic Effects in Terrestrial Meteorite Impact Structures: Lunar and Planetary Institute Contribution 954, 130 p.

Glass, B.P., and Simonson, B.M., 2012, Distal impact ejecta layers: Spherules and more: Elements, v. 8, no. 1, p. 43–48, https://doi.org/10.2113/gselements.8.1.43.

Goderis, S., Paquay, F., and Claeys, Ph., 2012, Projectile identification in terrestrial impact structures and ejecta material, *in* Osinski, G.R., and Pierazzo, E., eds., Impact Cratering: Processes and Products (1st ed.): Oxford, UK, Wiley-Blackwell, ch. 15, p. 223–239, https://doi.org/10.1002/9781118447307.ch15.

Goderis, S., Simonson, B.M., McDonald, I., Hassler, S.W., Izmer, A., Belza, J., Terryn, H., Vanhaecke, F., and Claeys, Ph., 2013a, Ni-rich spinels and platinum group element nuggets condensed from a late Archaean impact vapour cloud: Earth and Planetary Science Letters, v. 376, p. 87–98, https://doi.org/10.1016/j.epsl.2013.06.027.

Goderis, S., Tagle, R., Belza, J., Smit, J., Montanari, A., Vanhaecke, F., Erzinger, J., and Claeys, Ph., 2013b, Reevaluation of siderophile element abundances and ratios across the Cretaceous-Paleogene (K-Pg) boundary: Implications for the nature of the projectile: Geochimica et Cosmochimica Acta, v. 120, p. 417–446, https://doi.org/10.1016/j.gca.2013.06.010.

Goderis, S., Tagle, R., Fritz, J., Bartoschewitz, R., and Artemieva, N., 2017, On the nature of the Ni-rich component in splash-form Australasian tektites: Geochimica et Cosmochimica Acta, v. 217, p. 28–50, https://doi.org/10.1016/j.gca.2017.08.013.

Graup, G., 1999, Carbonate-silicate liquid immiscibility upon impact melting: Ries Crater, Germany: Meteoritics & Planetary Science, v. 34, no. 3, p. 425–438, https://doi.org/10.1111/j.1945-5100.1999.tb01351.x.

Grieve, R.A.F., and Therriault, A.M., 2012, Impactites: Their characteristics and spatial distribution, *in* Osinski, G.R., and Pierazzo, E., eds., Impact Cratering: Processes and Products (1st ed.): Oxford, UK, Wiley-Blackwell, ch. 7, p. 90–105, https://doi.org/10.1002/9781118447307.ch7.

Grieve, R.A.F., Palme, H., and Plant, A.G., 1981, Siderophile-rich particles in the melt rocks at the E. Clearwater impact structure, Quebec: Their characteristics and relationship to the impacting body: Contributions to Mineralogy and Petrology, v. 75, no. 3, p. 187–198, https://doi.org/10.1007/BF01166759.

Grieve, R.A.F., Ames, D.E., Morgan, J.V., and Artemieva, N., 2010, The evolution of the Onaping Formation at the Sudbury impact structure: Meteoritics & Planetary Science, v. 45, no. 5, p. 759–782, https://doi.org/10.1111/j.1945-5100.2010.01057.x.

Gulick, S.P.S., Bralower, T.J., Ormö, J., Hall, B., Grice, K., Schaefer, B., Lyons, S., Freeman, K.H., Morgan, J.V., Artemieva, N., Kaskes, P., de Graaff, S.J., Whalen, M.T., Collins, G.S., Tikoo, S.M., Verhagen, C., Christeson, G.L., Claeys, Ph., Coolen, M.J.L., Goderis, S., Goto, K., Grieve, R.A.F., McCall, N., Osinski, G.R., Rae, A.S.P., Riller, U., Smit, J., Vajda, V., Wittmann, A., and the Expedition 364 Scientists, 2019, The first day of the Cenozoic: Proceedings of the National Academy of Sciences of the United States of America, v. 116, no. 39, p. 19,342–19,351, https://doi.org/10.1073/pnas.1909479116.

Henke, B.L., Gullikson, E.M., and Davis, J.C., 1993, X-ray interactions: Photoabsorption, scattering, transmission, and reflection at E = 50–30000 eV, Z = 1–92: Atomic Data and Nuclear Data Tables, v. 54, no. 2, p. 181–342, https://doi.org/10.1006/adnd.1993.1013.

Hildebrand, A.R., Penfield, G.T., Kring, D.A., Pilkington, M., Camargo, Z.A., Jacobsen, S.B., and Boynton, W.V., 1991, Chicxulub Crater: A possible Cretaceous/Tertiary boundary impact crater on the Yucatán Peninsula, Mexico: Geology, v. 19, no. 9, p. 867–871, https://doi.org/10.1130/0091-7613(1991)019<0867:CCAPCT>2.3.CO;2.

Hoehnel, D., Reimold, W.U., Altenberger, U., Hofmann, A., Mohr-Westheide, T., Özdemir, S., and Koeberl, C., 2018, Petrographic and micro-XRF analysis of multiple Archean impact-derived spherule layers in drill core CT3 from the northern Barberton greenstone belt (South Africa): Journal of African Earth Sciences, v. 138, p. 264–288, https://doi.org/10.1016/j.jafrearsci.2017.11.020.

Hörz, F., Ostertag, R., and Rainey, D.A., 1983, Bunte Breccia of the Ries: Continuous deposits of large impact craters: Reviews of Geophysics, v. 21, no. 8, p. 1667–1725, https://doi.org/10.1029/RG021i008p01667.

Huber, M.S., Koeberl, C., Smith, F.C., Glass, B.P., Mundil, R., and McDonald, I., 2019, Geochemistry of a confirmed Precambrian impact ejecta deposit: The Grænsesø spherule layer, South Greenland: Meteoritics & Planetary Science, v. 54, no. 10, p. 2254–2272, https://doi.org/10.1111/maps.13271.

Jahn, B.-M., Floran, R.J., and Simonds, C.H., 1978, Rb-Sr isochron age of the Manicouagan melt sheet, Quebec, Canada: Journal of Geophysical Research–Solid Earth, v. 83, no. B6, p. 2799–2803, https://doi.org/10.1029/JB083iB06p02799.

Keppie, J.D., Dostal, J., Norman, M., Urrutia-Fucugauchi, J., and Grajales-Nishimura, M., 2011, Study of melt and a clast of 546 Ma magmatic arc rocks in the 65 Ma Chicxulub bolide breccia, northern Maya block, Mexico: Western limit of Ediacaran arc peripheral to northern Gondwana: International Geology Review, v. 53, no. 10, p. 1180–1193, https://doi.org/10.1080/00206810903545527.

Kettrup, B., and Deutsch, A., 2003, Geochemical variability of the Yucatàn basement: Constraints from crystalline clasts in Chicxulub impactites: Meteoritics & Planetary Science, v. 38, no. 7, p. 1079–1092, https://doi.org/10.1111/j.1945-5100.2003.tb00299.x.

Kettrup, B., Deutsch, A., and Masaitis, V.L., 2003, Homogeneous impact melts produced by a heterogeneous target? Sr-Nd isotopic evidence from the Popigai crater, Russia: Geochimica et Cosmochimica Acta, v. 67, no. 4, p. 733–750, https://doi.org/10.1016/S0016-7037(02)01143-2.

Koeberl, C., Shukolyukov, A., and Lugmair, G.W., 2007, Chromium isotopic studies of terrestrial impact craters: Identification of meteoritic components at Bosumtwi, Clearwater East, Lappajärvi, and Rochechouart: Earth and Planetary Science Letters, v. 256, no. 3–4, p. 534–546, https://doi.org/10.1016/j.epsl.2007.02.008.

Kring, D.A., 2005, Hypervelocity collisions into continental crust composed of sediments and an underlying crystalline basement: Comparing the Ries (~24 km) and Chicxulub (~180 km) impact craters: Geochemistry, v. 65, no. 1, p. 1–46, https://doi.org/10.1016/j.chemer.2004.10.003.

Kring, D.A., Claeys, Ph., Gulick, S.P.S., Morgan, J.V., Collins, G.S., and the IODP-ICDP Expedition 364 Science Party, 2017, Chicxulub and the exploration of large peak-ring impact craters through scientific drilling: GSA Today, v. 27, no. 10, p. 4–8, https//doi.org/10.1130/GSATG352A.1.

Kring, D.A., Tikoo, S.M., Schmieder, M., Riller, U., Rebolledo-Vieyra, M., Simpson, S.L., Osinski, G.R., Gattacceca, J., Wittmann, A., Verhagen, C.M., Cockell, C.S., Coolen, M.J.L., Longstaffe, F.J., Gulick, S.P.S., Morgan, J.V., Bralower, T.J., Chenot, E., Christeson, G.L., Claeys, Ph., Ferrière, L., Gebhardt, C., Goto, K., Green, S.L., Jones, H., Lofi, J., Lowery, C.M., Ocampo-Torres, R., Perez-Cruz, L., Pickersgill, A.E., Poelchau, M.H., Rae, A.S.P., Rasmussen, C., Sato, H., Smit, J., Tomioka, N., Urrutia-Fucugauchi, J., Whalen, M.T., Xiao, L., and Yamaguchi, K.E., 2020, Probing the hydrothermal system of the Chicxulub impact crater: Science Advances, v. 6, no. 22, p. eaaz3053, https://doi.org/10.1126/sciadv.aaz3053.

Kyte, F.T., Shukolyukov, A., Hildebrand, A.R., Lugmair, G.W., and Hanova, J., 2011, Chromium-isotopes in late Eocene impact spherules indicate a likely asteroid belt provenance: Earth and Planetary Science Letters, v. 302, no. 3–4, p. 279–286, https://doi.org/10.1016/j.epsl.2010.12.006.

Laforce, B., 2018, Development of Laboratory and Synchrotron Based 2D/3D XRF Techniques for Multidisciplinary Research [Ph.D. thesis]: Ghent, Belgium, Universiteit Gent, 228 p.

Lambert, P., 1975, Nickel enrichment of impact melt rocks from Rochechouart: Preliminary results and possibility of meteoritic contamination: Meteoritics, v. 10, p. 433–436.

Liu, S., Glass, B.P., Kyte, F.T., and Bohaty, S.M., 2009, The late Eocene clinopyroxene-bearing spherule layer: New sites, nature of the strewn field, Ir data, and discovery of coesite and shocked quartz, *in* Koeberl, C., and Montanari, A., eds, The Late Eocene Earth—Hothouse, Icehouse, and Impacts: Geological Society of America Special Paper 452, p. 37–70, https://doi.org/10.1130/2009.2452(04).

Lutz, B.G., 1985, The Metamorphism in the Mobile Belts of the Early Earth: Moscow, Nauka Press, 216 p. [in Russian].

Marchand, M., and Crocket, J.H., 1977, Sr isotopes and trace element geochemistry of the impact melt and target rocks at the Mistastin Lake crater, Labrador: Geochimica et Cosmochimica Acta, v. 41, no. 10, p. 1487–1495, https://doi.org/10.1016/0016-7037(77)90253-8.

Masaitis, V.L., 1994, Impactites from Popigai crater, *in* Dressler, B.O., Grieve, R.A.F., and Sharpton, V.L., eds., Large Meteorite Impacts and Planetary Evolution: Geological Society of America Special Paper 293, p. 153–162, https://doi.org/10.1130/SPE293-p153.

Masaitis, V.L., 2003, Obscure-bedded ejecta facies from the Popigai impact structure, Siberia: Lithological features and mode of origin, *in* Koeberl, C., and Martínez-Ruiz, F.C., eds., Impact Markers in the Stratigraphic Record: Impact Studies: Berlin, Springer, p. 137–162, https://doi.org/10.1007/978-3-642-55463-6_6.

Masaitis, V.L., Naumov, M.V., and Mashchak, M.S., 2005, Original diameter and depth of erosion of the Popigai impact crater, Russia, *in* Kenkmann, T., Hörz, F., and Deutsch, A., eds., Large Meteorite Impacts III: Geological Society of America Special Paper 384, p. 131–140, https://doi.org/10.1130/0-8137-2384-1.131.

Masaitis, V.L., Petrov, O.V., and Naumov, M.V., 2018, Impact lithologies—A key for reconstruction of rock-forming processes and a geological model of the Popigai crater, northern Siberia: Australian Journal of Earth Sciences, v. 66, no. 1, p. 81–94, https://doi.org/10.1080/08120099.2018.1509372.

Melosh, H.J., 1989, Impact Cratering: A Geologic Process: Oxford Monographs on Geology and Geophysics 11, 253 p.

Morgan, J.V., Gulick, S.P.S., Bralower, T.J., Chenot, E., Christeson, G.L., Claeys, Ph., Cockell, C.S., Collins, G.S., Coolen, M.J.L., Ferrière, L., Gebhardt, C., Goto, K., Jones, H., Kring, D.A., Le Ber, E., Lofi, J., Xiao, L., Lowery, C.M., Mellett, C.L., Ocampo-Torres, R., Osinski, G.R., Perez-Cruz, L., Pickersgill, A.E., Poelchau, M.H., Rae, A.S.P., Rasmussen, C., Rebolledo-Vieyra, M., Riller, U., Sato, H., Schmitt, D.R., Smit, J., Tikoo, S.M., Tomioka, N., Urrutia-Fucugauchi, J., Whalen, M.T., Wittmann, A., Yamaguchi, K.E., and Zylberman, W., 2016, The formation of peak rings in large impact craters: Science, v. 354, no. 6314, p. 878–882, https://doi.org/10.1126/science.aah6561.

Morgan, J.V., Gulick, S.P.S., Mellett, C.L., Green, S.L., and the Expedition 364 Scientists, 2017, Chicxulub: Drilling the K-Pg Impact Crater: Proceedings of the International Ocean Discovery Program, Volume 364: College Station, Texas, International Ocean Discovery Program, https//doi.org/10.14379/iodp.proc.364.2017.

Naumov, M.V., 2002, Impact-generated hydrothermal systems: Data from Popigai, Kara, and Puchezh-Katunki impact structures, *in* Plado, J., and Pesonen, L.J., eds., Impacts in Precambrian Shields: Impact Studies: Berlin, Springer, p. 117–171, https://doi.org/10.1007/978-3-662-05010-1_6.

Ormö, J., Sturkell, E., and Lindström, M., 2007, Sedimentological analysis of resurge deposits at the Lockne and Tvären craters: Clues to flow dynamics: Meteoritics & Planetary Science, v. 42, no. 11, p. 1929–1943, https://doi.org/10.1111/j.1945-5100.2007.tb00551.x.

Osinski, G.R., 2003, Impact glasses in fallout suevites from the Ries impact structure, Germany: An analytical SEM study: Meteoritics & Planetary Science, v. 38, no. 11, p. 1641–1667, https://doi.org/10.1111/j.1945-5100.2003.tb00006.x.

Osinski, G.R., Grieve, R.A.F., and Spray, J.G., 2004, The nature of the groundmass of surficial suevite from the Ries impact structure, Germany, and constraints on its origin: Meteoritics & Planetary Science, v. 39, no. 10, p. 1655–1683, https://doi.org/10.1111/j.1945-5100.2004.tb00065.x.

Osinski, G.R., Grieve, R.A.F., Collins, G.S., Marion, C., and Sylvester, P., 2008, The effect of target lithology on the products of impact melting: Meteoritics & Planetary Science, v. 43, no. 12, p. 1939–1954, https://doi.org/10.1111/j.1945-5100.2008.tb00654.x.

Osinski, G.R., Grieve, R.A.F., Hill, P.J.A., Simpson, S.L., Cockell, C.S., Christeson, G.L., Ebert, M., Gulick, S.P.S., Melosh, H.J., Riller, U., Tikoo, S.M., and Wittmann, A., 2020, Explosive interaction of impact melt and seawater following the Chicxulub impact event: Geology, v. 48, no. 2, p. 108–112, https://doi.org/10.1130/G46783.1.

Pittarello, L., and Koeberl, C., 2013, Clast size distribution and quantitative petrography of shocked and unshocked rocks from the El'gygytgyn impact structure: Meteoritics & Planetary Science, v. 48, no. 7, p. 1325–1338, https://doi.org/10.1111/maps.12070.

Pohl, J., Stöffler, D., Gall, H., and Ernstson, K., 1977, The Ries impact crater, *in* Roddy, D.J., Pepin, R.O., and Merrill, R.B., eds., Impact and Explosion Cratering: New York, Pergamon Press, p. 343–404.

Poppe, S., Galland, O., de Winter, N.J., Goderis, S., Claeys, Ph., Debaille, V., Boulvais, P., and Kervyn, M., 2020, Structural and geochemical interactions between magma and sedimentary host rock: The Hovedøya case, Oslo Rift, Norway: Geochemistry, Geophysics, Geosystems, v. 21, no. 3, p. e2019GC008685, https//doi.org/10.1029/2019gc008685.

Potts, P.J., and Webb, P.C., 1992, X-ray fluorescence spectrometry: Journal of Geochemical Exploration, v. 44, no. 1–3, p. 251–296, https://doi.org/10.1016/0375-6742(92)90052-A.

Rabkin, M.I., 1959, The Geology and Petrology of the Anabar Shield: Proceedings of the Arctic Geology Research Institute (NIIGA), v. 87, 164 p. [in Russian].

Raikhlin, A.I., 1996, Suevites of the Popigai impact crater: Internal structure and condition of formation: Solar System Research, v. 30, p. 14–18.

Reed, S.J.B., 2005, Electron Microprobe Analysis and Scanning Electron Microscopy in Geology (2nd ed.): Cambridge, UK, Cambridge University Press, 189 p., https://doi.org/10.1017/CBO9780511610561.

Reimold, W.U., Barr, J.M., Grieve, R.A.F., and Durrheim, R.J., 1990, Geochemistry of the melt and country rocks of the Lake St. Martin impact structure, Manitoba, Canada: Geochimica et Cosmochimica Acta, v. 54, no. 7, p. 2093–2111, https://doi.org/10.1016/0016-7037(90)90273-N.

Renne, P.R., Deino, A.L., Hilgen, F.J., Kuiper, K.F., Mark, D.F., Mitchell, W.S., III, Morgan, L.E., Mundil, R., and Smit, J., 2013, Time scales of critical events around the Cretaceous-Paleogene boundary: Science, v. 339, no. 6120, p. 684–687, https://doi.org/10.1126/science.1230492.

Riller, U., Poelchau, M.H., Rae, A.S.P., Schulte, F.M., Collins, G.S., Melosh, H.J., Grieve, R.A.F., Morgan, J.V., Gulick, S.P.S., Lofi, J., Diaw, A., McCall, N., Kring, D.A., and IODP–ICDP Expedition 364 Science Party, 2018, Rock fluidization during peak-ring formation of large impact structures: Nature, v. 562, p. 511–518, https://doi.org/10.1038/s41586-018-0607-z.

Rousseau, R.M., 1984a, Fundamental algorithm between concentration and intensity in XRF analysis 1—Theory: X-Ray Spectrometry, v. 13, no. 3, p. 115–120, https://doi.org/10.1002/xrs.1300130306.

Rousseau, R.M., 1984b, Fundamental algorithm between concentration and intensity in XRF analysis 2—Practical application: X-Ray Spectrometry, v. 13, no. 3, p. 121–125, https://doi.org/10.1002/xrs.1300130307.

Rousseau, R.M., and Boivin, J.A., 1998, The fundamental algorithm: A natural extension of the Sherman equation: Part I. Theory: The Rigaku Journal, v. 15, no. 1, p. 13–28.

Rousseau, R.M., and Bouchard, M., 1986, Fundamental algorithm between concentration and intensity in XRF analysis 3—Experimental verification: X-Ray Spectrometry, v. 15, no. 3, p. 207–215, https://doi.org/10.1002/xrs.1300150311.

Schmidt-Kaler, H., 1978, Geological setting and history, *in* Chao, E.C.T., Hüttner, R., and Schmidt-Kaler, H., eds, Principal Exposures of the Ries Meteorite Crater in Southern Germany: Munich, Germany, Bayerisches Geologisches Landesamt, p. 8–11.

Schmieder, M., and Kring, D.A., 2020, Earth's impact events through geologic time: A list of recommended ages for terrestrial impact structures and deposits: Astrobiology, v. 20, no. 1, p. 91–141, https://doi.org/10.1089/ast.2019.2085.

Schmieder, M., Kennedy, T., Jourdan, F., Buchner, E., and Reimold, W.U., 2018, A high-precision $^{40}Ar/^{39}Ar$ age for the Nördlinger Ries impact crater, Germany, and implications for the accurate dating of terrestrial impact events: Geochimica et Cosmochimica Acta, v. 220, p. 146–157, https://doi.org/10.1016/j.gca.2017.09.036.

Shackley, M.S., ed., 2011, X-Ray Fluorescence Spectrometry (XRF) in Geoarchaeology: New York, Springer, 243 p., https://doi.org/10.1007/978-1-4419-6886-9.

Sherman, J., 1955, The theoretical derivation of fluorescent X-ray intensities from mixtures: Spectrochimica Acta, v. 7, p. 283–306, https://doi.org/10.1016/0371-1951(55)80041-0.

Siegert, S., and Hecht, L., 2018, Heterogeneity of melts in impact deposits and implications for their origin (Ries suevite, Germany): Meteoritics & Planetary Science, v. 54, no. 10, p. 2409–2447, https://doi.org/10.1111/maps.13210.

Siegert, S., Branney, M.J., and Hecht, L., 2017, Density current origin of a melt-bearing impact ejecta blanket (Ries suevite, Germany): Geology, v. 45, no. 9, p. 855–858, https://doi.org/10.1130/G39198.1.

Simonds, C.H., and Kieffer, S.W., 1993, Impact and volcanism: A momentum scaling law for erosion: Journal of Geophysical Research–Solid Earth, v. 98, no. B8, p. 14,321–14,337, https://doi.org/10.1029/93JB00704.

Simpson, S.L., Osinski, G.R., Longstaffe, F.J., Schmieder, M., and Kring, D.A., 2020, Hydrothermal alteration associated with the Chicxulub impact crater upper peak-ring breccias: Earth and Planetary Science Letters, v. 547, 116425, https://doi.org/10.1016/j.epsl.2020.116425.

Sprain, C.J., Renne, P.R., Clemens, W.A., and Wilson, G.P., 2018, Calibration of chron C29r: New high-precision geochronologic and paleomagnetic constraints from the Hell Creek region, Montana: Geological Society of America Bulletin, v. 130, no. 9–10, p. 1615–1644, https://doi.org/10.1130/B31890.1.

Stöffler, D., 1977, Research drilling Nördlingen 1973: Polymict breccias, crater basement, and cratering model of the Ries impact structure: Geologica Bavarica, v. 75, p. 443–458.

Stöffler, D., and Grieve, R.A.F., 2007, Impactites, *in* Fettes, D., and Desmons, J., eds., Metamorphic Rocks: A Classification and Glossary of Terms, Recommendations of the International Union of Geological Sciences Subcommission on the Systematics of Metamorphic Rocks: Cambridge, UK, Cambridge University Press, ch. 2.11, p. 82–92, 111–125, and 126–242.

Stöffler, D., Artemieva, N.A., Wünnemann, K., Reimold, W.U., Jacob, J., Hansen, B.K., and Summerson, I.A.T., 2013, Ries crater and suevite revisited—Observations and modeling: Part I. Observations: Meteoritics & Planetary Science, v. 48, no. 4, p. 515–589, https://doi.org/10.1111/maps.12086.

Tagle, R., 2004, Platingruppenelemente in Meteoriten und Gesteinen irdischer Impaktkrater: Identifizierung der Einschlagskörper [Ph.D. thesis]: Berlin, Germany, Humboldt Universität, 173 p. [in German].

Tagle, R., and Berlin, J., 2008, A database of chondrite analyses including platinum group elements, Ni, Co, Au, and Cr: Implications for the identification of chondritic projectiles: Meteoritics & Planetary Science, v. 43, no. 3, p. 541–559, https://doi.org/10.1111/j.1945-5100.2008.tb00671.x.

Tagle, R., and Claeys, Ph., 2005, An ordinary chondrite impactor for the Popigai crater, Siberia: Geochimica et Cosmochimica Acta, v. 69, no. 11, p. 2877–2889, https://doi.org/10.1016/j.gca.2004.11.024.

Tagle, R., Erzinger, J., Hecht, L., Schmitt, R.T., Stöffler, D., and Claeys, Ph., 2004, Platinum group elements in impactites of the ICDP Chicxulub drill core Yaxcopoil-1: Are there traces of the projectile?: Meteoritics & Planetary Science, v. 39, no. 6, p. 1009–1016. https://doi.org/10.1111/j.1945-5100.2004.tb00942.x.

Thompson, L.M., and Spray, J.G., 2017, Dynamic interaction between impact melt and fragmented basement at Manicouagan: The suevite connection: Meteoritics & Planetary Science, v. 52, no. 7, p. 1300–1329, https://doi.org/10.1111/maps.12889.

Urrutia-Fucugauchi, J., Camargi-Zanoguera, A., Pérez-Cruz, L., and Pérez-Cruz, G., 2011, The Chicxulub multi-ring impact crater, Yucatan carbonate platform, Gulf of Mexico: Geofísica Internacional, v. 50, no. 1, p. 99–127.

Van Malderen, S.J.M., 2017, Optimization of Methods Based on Laser Ablation–ICP–Mass Spectrometry (LA-ICP-MS) for 2-D and 3-D Elemental Mapping [Ph.D. thesis]: Ghent, Belgium, Universiteit Gent, 303 p.

Vansteenberge, S., de Winter, N.J., Sinnesael, M., Xueqin, Z., Verheyden, S., and Claeys, Ph., 2020, Benchtop μXRF as a tool for speleothem trace elemental analysis: Validation, limitations and application on an Eemian to early Weichselian (125–97 ka) stalagmite from Belgium: Palaeogeography, Palaeoclimatology, Palaeoecology, v. 538, 109460, https://doi.org/10.1016/j.palaeo.2019.109460.

Vishnevsky, S., and Montanari, A., 1999, Popigai impact structure (Arctic Siberia, Russia): Geology, petrology, geochemistry, and geochronology of glass-bearing impactites, *in* Dressler, B.O., and Sharpton, V.L., eds., Large Meteorite Impacts and Planetary Evolution II: Geological Society of America Special Paper 339, p. 19–59, https://doi.org/10.1130/0-8137-2339-6.19.

von Engelhardt, W., and Graup, G., 1984, Suevite of the Ries crater, Germany: Source rocks and implications for cratering mechanics: Geologische Rundschau, v. 73, p. 447–481, https://doi.org/10.1007/BF01824968.

Whitehead, J., Grieve, R.A.F., and Spray, J.G., 2002, Mineralogy and petrology of melt rocks from the Popigai impact structure, Siberia: Meteoritics & Planetary Science, v. 37, no. 5, p. 623–647, https://doi.org/10.1111/j.1945-5100.2002.tb00844.x.

Wittmann, A., Kenkmann, T., Hecht, L., and Stöffler, D., 2007, Reconstruction of the Chicxulub ejecta plume from its deposits in drill core Yaxcopoil-1: Geological Society of America Bulletin, v. 119, no. 9–10, p. 1151–1167, https://doi.org/10.1130/B26116.1.

Zhao, J., Xiao, L., Gulick, S.P.S., Morgan, J.V., Kring, D.A., Urrutia-Fucugauchi, J., Schmieder, M., de Graaff, S.J., Wittmann, A., Ross, C.H., Claeys, Ph., Pickersgill, A.E., Kaskes, P., Goderis, S., Rasmussen, C., Vajda, V., Ferrière, L., Feignon, J–G., Chenot, E., Perez-Cruz, L., Sato, H., Yamaguchi, K.E., and IODP–ICDP Expedition 364 scientists, 2020, Geochemistry, geochronology and petrogenesis of Maya block granitoids and dykes from the Chicxulub impact crater, Gulf of México: Implications for the assembly of Pangea: Gondwana Research, v. 82, p. 128–150, https://doi.org/10.1016/j.gr.2019.12.003.

Manuscript Accepted by the Society 20 November 2020
Manuscript Published Online 16 April 2021

Printed in the USA